

Combined Analysis of all Three Phases of Solar Neutrino Data from the Sudbury Neutrino Observatory

B. Aharmim,⁶ S.N. Ahmed,¹⁴ A.E. Anthony,^{17, a} N. Barros,^{8, b} E.W. Beier,¹³ A. Bellerive,⁴ B. Beltran,¹ M. Bergevin,^{7, 5, c} S.D. Biller,¹² K. Boudjemline,^{4, 14} M.G. Boulay,¹⁴ B. Cai,¹⁴ Y.D. Chan,⁷ D. Chauhan,⁶ M. Chen,¹⁴ B.T. Cleveland,¹² G.A. Cox,^{19, d} X. Dai,^{14, 12, 4} H. Deng,¹³ J.A. Detwiler,⁷ M. DiMarco,¹⁴ P.J. Doe,¹⁹ G. Doucas,¹² P.-L. Drouin,⁴ F.A. Duncan,^{16, 14} M. Dunford,^{13, e} E.D. Earle,¹⁴ S.R. Elliott,^{9, 19} H.C. Evans,¹⁴ G.T. Ewan,¹⁴ J. Farine,^{6, 4} H. Fergani,¹² F. Fleurot,⁶ R.J. Ford,^{16, 14} J.A. Formaggio,^{11, 19} N. Gagnon,^{19, 9, 7, 12} J.T.M. Goon,¹⁰ K. Graham,^{4, 14} E. Guillian,¹⁴ S. Habib,¹ R.L. Hahn,³ A.L. Hallin,¹ E.D. Hallman,⁶ P.J. Harvey,¹⁴ R. Hazama,^{19, f} W.J. Heintzelman,¹³ J. Heise,^{2, 9, 14, g} R.L. Helmer,¹⁸ A. Hime,⁹ C. Howard,^{1, h} M. Huang,^{17, 6, i} P. Jagam,⁵ B. Jamieson,² N.A. Jelley,¹² M. Jerkins,¹⁷ K.J. Keeter,¹⁴ J.R. Klein,^{17, 13} L.L. Kormos,¹⁴ M. Kos,¹⁴ C. Kraus,^{14, 6} C.B. Krauss,¹ A. Kruger,⁶ T. Kutter,¹⁰ C.C.M. Kyba,^{13, j} R. Lange,³ J. Law,⁵ I.T. Lawson,^{16, 5} K.T. Lesko,⁷ J.R. Leslie,¹⁴ J.C. Loach,^{12, 7} R. MacLellan,^{14, k} S. Majerus,¹² H.B. Mak,¹⁴ J. Maneira,⁸ R. Martin,^{14, 7} N. McCauley,^{13, 12, 1} A.B. McDonald,¹⁴ S.R. McGee,¹⁹ M.L. Miller,^{11, m} B. Monreal,^{11, n} J. Monroe,^{11, o} B.G. Nickel,⁵ A.J. Noble,^{14, 4} H.M. O’Keeffe,¹² N.S. Oblath,^{19, 11} R.W. Ollerhead,⁵ G.D. Orebi Gann,^{12, 13, p} S.M. Oser,² R.A. Ott,¹¹ S.J.M. Peeters,^{12, q} A.W.P. Poon,⁷ G. Prior,^{7, e} S.D. Reitzner,⁵ K. Rielage,^{9, 19} B.C. Robertson,¹⁴ R.G.H. Robertson,¹⁹ R.C. Rosten,¹⁹ M.H. Schwendener,⁶ J.A. Secrest,^{13, r} S.R. Seibert,^{17, 9, 13} O. Simard,^{4, s} J.J. Simpson,⁵ P. Skensved,¹⁴ T.J. Sonley,^{11, t} L.C. Stonehill,^{9, 19} G. Tešić,^{4, u} N. Tolich,¹⁹ T. Tsui,² R. Van Berg,¹³ B.A. VanDevender,^{19, v} C.J. Virtue,⁶ H. Wan Chan Tseung,^{12, 19} D.L. Wark,^{15, w} P.J.S. Watson,⁴ J. Wendland,² N. West,¹² J.F. Wilkerson,^{19, h} J.R. Wilson,^{12, x} J.M. Wouters,^{9, y} A. Wright,^{14, z} M. Yeh,³ F. Zhang,⁴ and K. Zuber^{12, b}

(SNO Collaboration)

¹*Department of Physics, University of Alberta, Edmonton, Alberta, T6G 2R3, Canada*

²*Department of Physics and Astronomy, University of British Columbia, Vancouver, BC V6T 1Z1, Canada*

³*Chemistry Department, Brookhaven National Laboratory, Upton, NY 11973-5000*

⁴*Ottawa-Carleton Institute for Physics, Department of Physics, Carleton University, Ottawa, Ontario K1S 5B6, Canada*

⁵*Physics Department, University of Guelph, Guelph, Ontario N1G 2W1, Canada*

⁶*Department of Physics and Astronomy, Laurentian University, Sudbury, Ontario P3E 2C6, Canada*

⁷*Institute for Nuclear and Particle Astrophysics and Nuclear Science*

Division, Lawrence Berkeley National Laboratory, Berkeley, CA 94720

⁸*Laboratório de Instrumentação e Física Experimental de Partículas, Av. Elias Garcia 14, 1^o, 1000-149 Lisboa, Portugal*

⁹*Los Alamos National Laboratory, Los Alamos, NM 87545*

¹⁰*Department of Physics and Astronomy, Louisiana State University, Baton Rouge, LA 70803*

¹¹*Laboratory for Nuclear Science, Massachusetts Institute of Technology, Cambridge, MA 02139*

¹²*Department of Physics, University of Oxford, Denys Wilkinson Building, Keble Road, Oxford OX1 3RH, UK*

¹³*Department of Physics and Astronomy, University of Pennsylvania, Philadelphia, PA 19104-6396*

¹⁴*Department of Physics, Queen’s University, Kingston, Ontario K7L 3N6, Canada*

¹⁵*Rutherford Appleton Laboratory, Chilton, Didcot OX11 0QX, UK*

¹⁶*SNOLAB, Sudbury, ON P3Y 1M3, Canada*

¹⁷*Department of Physics, University of Texas at Austin, Austin, TX 78712-0264*

¹⁸*TRIUMF, 4004 Wesbrook Mall, Vancouver, BC V6T 2A3, Canada*

¹⁹*Center for Experimental Nuclear Physics and Astrophysics, and*

Department of Physics, University of Washington, Seattle, WA 98195

We report results from a combined analysis of solar neutrino data from all phases of the Sudbury Neutrino Observatory. By exploiting particle identification information obtained from the proportional counters installed during the third phase, this analysis improved background rejection in that phase of the experiment. The combined analysis resulted in a total flux of active neutrino flavors from ⁸B decays in the Sun of $(5.25 \pm 0.16(\text{stat.})_{-0.13}^{+0.11}(\text{syst.})) \times 10^6 \text{ cm}^{-2}\text{s}^{-1}$. A two-flavor neutrino oscillation analysis yielded $\Delta m_{21}^2 = (5.6_{-1.4}^{+1.9}) \times 10^{-5} \text{ eV}^2$ and $\tan^2 \theta_{12} = 0.427_{-0.029}^{+0.033}$. A three-flavor neutrino oscillation analysis combining this result with results of all other solar neutrino experiments and the KamLAND experiment yielded $\Delta m_{21}^2 = (7.41_{-0.19}^{+0.21}) \times 10^{-5} \text{ eV}^2$, $\tan^2 \theta_{12} = 0.446_{-0.029}^{+0.030}$, and $\sin^2 \theta_{13} = (2.5_{-1.5}^{+1.8}) \times 10^{-2}$. This implied an upper bound of $\sin^2 \theta_{13} < 0.053$ at the 95% confidence level (C.L.).

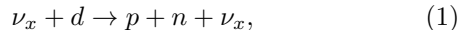
I. INTRODUCTION

The Sudbury Neutrino Observatory (SNO) was designed to measure the flux of neutrinos produced by ⁸B

decays in the Sun, so-called ⁸B neutrinos, and to study neutrino oscillations, as proposed by Herb Chen [1]. As a result of measurements with the SNO detector and other

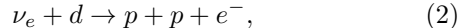
experiments, it is now well-established that neutrinos are massive and that the weak eigenstates (ν_e, ν_μ, ν_τ) are mixtures of the mass eigenstates (ν_1, ν_2, ν_3). The probability of detecting a neutrino in the same weak eigenstate in which it was created depends on the energy and propagation distance of the neutrino, the effects of matter [2, 3], the neutrino mixing angles ($\theta_{12}, \theta_{23}, \theta_{13}$), a phase (δ) which can lead to charge-parity violation, and the differences between the squares of the neutrino mass eigenvalues ($\Delta m_{21}^2, \Delta m_{32}^2, \Delta m_{31}^2$) [4, 5].

The SNO detector observed ^8B neutrinos via three different reactions. By measuring the rate of neutral current (NC) reactions,



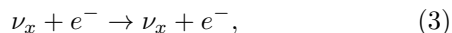
which is equally sensitive to all three active neutrino flavors, the SNO experiment determined the total ^8B neutrino flux, Φ_{B} , independently of any specific active neutrino flavor oscillation hypothesis [1]. The predicted flux from solar model calculations [6] is $(5.88 \pm 0.65) \times 10^6 \text{ cm}^{-2}\text{s}^{-1}$, BPS09(GS), or $(4.85 \pm 0.58) \times 10^6 \text{ cm}^{-2}\text{s}^{-1}$, BPS09(AGSS09), using a recent measurement of the heavy-element abundance at the Sun's surface. Previous analyses of SNO data [7, 8] measured Φ_{B} more precisely than the solar model predictions. A more precise measurement of Φ_{B} would better constrain these solar models, but may not necessarily determine which metallicity is correct due to the large uncertainties at present on both predictions.

By measuring the rate of charged current (CC) reactions,



which is only sensitive to ν_e s, and comparing this to the NC reaction rate, it was possible to determine the neutrino survival probability as a function of energy. This can then constrain the neutrino oscillation parameters independently of any specific prediction of Φ_{B} .

The SNO experiment also measured the rate of elastic scattering (ES) reactions,



which is sensitive to all neutrino flavors, but the cross-section for ν_e s is approximately six times larger than that for the other flavors.

We present in this article a final combined analysis of all solar neutrino data from the SNO experiment. Section II gives an overview of the detector. In Section III we describe the method used to combine all the data in a fit which determines Φ_{B} and a parameterized form of the ν_e survival probability. Section IV describes a new particle identification technique that allowed us to significantly suppress the background events in the proportional counters used in the third phase of the SNO experiment. Section V presents the results of the new analysis of data from Phase III, and the combined analysis of data from all phases. The results of this combined analysis are interpreted in the context of neutrino oscillations in Section VI.

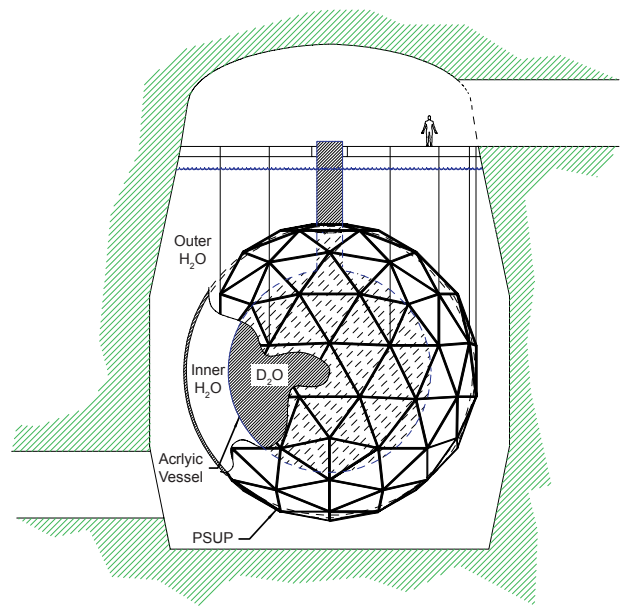


FIG. 1. Schematic diagram of the SNO detector. We used a coordinate system with the center of the detector as the origin, and z direction as vertically upward.

II. THE SNO DETECTOR

The SNO detector [9], shown schematically in Figure 1, consisted of an inner volume containing 10^6 kg of 99.92% isotopically pure heavy water ($^2\text{H}_2\text{O}$, hereafter referred to as D_2O) within a 12 m diameter transparent acrylic vessel (AV). Over 7×10^6 kg of H_2O between the rock and the AV shielded the D_2O from external radioactive backgrounds. An array of 9456 inward-facing 20 cm Hamamatsu R1408 photomultiplier tubes (PMTs), installed on an 17.8 m diameter stainless steel geodesic structure (PSUP), detected Cherenkov radiation produced in both the D_2O and H_2O . A non-imaging light concentrator [10] mounted on each PMT increased the effective photocathode coverage to nearly 55% of 4π . The PMT thresholds were set to $1/4$ of the charge from a single photoelectron. The inner 1.7×10^6 kg of H_2O between the AV and the PSUP shielded the D_2O against radioactive backgrounds from the PSUP and PMTs. Extensive purification systems removed radioactive isotopes from both the D_2O and the H_2O [11].

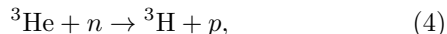
The detector was located in Vale's Creighton mine ($46^\circ 28' 30''$ N latitude, $81^\circ 12' 04''$ W longitude) near Sudbury, Ontario, Canada, with the center of the detector at a depth of 2092 m (5890 ± 94 meters water equivalent). At this depth, the rate of cosmic-ray muons entering the detector was approximately three per hour. Ninety-one outward-facing PMTs attached to the PSUP detected cosmic-ray muons. An offline veto based on information from these PMTs significantly reduced cosmogenic backgrounds.

The recoil electrons from both the ES and CC reac-

tions were detected directly through their production of Cherenkov light. The total amount of light detected by the PMT array was correlated with the energy of the interacting neutrino.

The SNO detector operated in three distinct phases distinguished by how the neutrons from the NC interactions were detected. In Phase I, the detected neutrons captured on deuterons in the D₂O releasing a single 6.25 MeV γ -ray, and it was the Cherenkov light of secondary Compton electrons or e^+e^- pairs that was detected. In Phase II, 2×10^3 kg of NaCl were added to the D₂O, and the neutrons captured predominantly on ³⁵Cl nuclei, which have a much larger neutron capture cross-section than deuterium nuclei, resulting in a higher neutron detection efficiency. Capture on chlorine also released more energy (8.6 MeV) and yielded multiple γ -rays, which aided in identifying neutron events. In Phase III, an array of proportional counters (the Neutral Current Detection, or NCD, array) was deployed in the D₂O [12].

The proportional counters were constructed of approximately 2 m long high purity nickel tubes welded together to form longer “strings”. Neutrons were detected via the reaction



where the triton and proton had a total kinetic energy of 0.76 MeV, and travelled in opposite directions. The NCD array consisted of 36 strings filled with ³He, and an additional 4 strings filled with ⁴He that were insensitive to the neutron signals and were used to study backgrounds. Energetic charged particles within the proportional counters produced ionization electrons, and the induced voltage caused by these electrons was recorded as a function of time, referred to as a waveform. To increase the dynamic range, the waveform was logarithmically amplified before being digitized [12].

III. COMBINED ANALYSIS

In this article we present an analysis that combines data from all three phases of the SNO experiment. The combination accounts for any correlations in the systematic uncertainties between phases. The data were split into day and night sets in order to search for matter effects as the neutrinos propagated through the Earth.

The general form of the analysis was a fit to Monte Carlo-derived probability density functions (PDFs) for each of the possible signal and background types. As with previous analyses of SNO data, the following four variables were calculated for each event recorded with the PMT array: the effective electron kinetic energy, T_{eff} , reconstructed under the hypothesis that the light was caused by a single electron; the cube of the radial position, r , divided by 600 cm, $\rho = (r[\text{cm}]/600)^3$; the isotropy of the detected light, β_{14} ; and the angle of the reconstructed electron propagation relative to the direction of

the Sun, $\cos\theta_{\odot}$. Different algorithms to calculate both T_{eff} and ρ were used for the first two phases and the third phase. References [7, 13, 14] contain detailed descriptions of how these variables were calculated. The energy deposited in the gas of a proportional counter, E_{NCD} , was calculated for each event recorded with the NCD array, and the correlated waveform was determined [14].

Although there were multiple sets of data in this fit, the result was a single Φ_{B} and energy-dependent ν_e survival probability as described in Section III.1. We summarize the event selection and backgrounds in Section III.2. Sections III.3 and III.4, respectively, describe the PDFs and efficiencies. The method for combining the multiple sets of data in a single analysis is presented in Section III.5. Finally, Section III.6 outlines the alternative analyses to verify the combined analysis.

III.1. Parameterization of the ⁸B neutrino signal

We fitted the neutrino signal based on an average Φ_{B} for day and night, a ν_e survival probability as a function of neutrino energy, E_{ν} , during the day, $P_{ee}^{\text{d}}(E_{\nu})$, and an asymmetry between the day and night survival probabilities, $A_{ee}(E_{\nu})$, defined by

$$A_{ee}(E_{\nu}) = 2 \frac{P_{ee}^{\text{n}}(E_{\nu}) - P_{ee}^{\text{d}}(E_{\nu})}{P_{ee}^{\text{n}}(E_{\nu}) + P_{ee}^{\text{d}}(E_{\nu})}, \quad (5)$$

where $P_{ee}^{\text{n}}(E_{\nu})$ was the ν_e survival probability during the night. This was the same parameterization as we used in our previous analysis of data from Phases I and II [7].

Monte Carlo simulations assuming the standard solar model and no neutrino oscillations were used to determine the event variables for ⁸B neutrino interactions in the detector. These simulations were then scaled by the factors given in Table I.

TABLE I. ⁸B neutrino interactions scaling factors.

Interaction	Day/Night	Scaling factor
CC, ES _e	Day	$\Phi_{\text{B}} P_{ee}^{\text{d}}(E_{\nu})$
ES _{$\mu\tau$}	Day	$\Phi_{\text{B}} [1 - P_{ee}^{\text{d}}(E_{\nu})]$
CC, ES _e	Night	$\Phi_{\text{B}} P_{ee}^{\text{n}}(E_{\nu})$
ES _{$\mu\tau$}	Night	$\Phi_{\text{B}} [1 - P_{ee}^{\text{n}}(E_{\nu})]$
NC	Day+Night	Φ_{B}

Unlike our earlier publications [8, 13, 15], this parameterization included a constraint on the rate of ES interactions relative to the rate of CC interactions based on their relative cross-sections. It also had the advantage that the fitted parameters (Φ_{B} , $P_{ee}^{\text{d}}(E_{\nu})$, and $A_{ee}(E_{\nu})$) were all directly related to the scientific questions under investigation. Moreover, it disentangled the detector response from the fit result as $P_{ee}^{\text{d}}(E_{\nu})$ and $A_{ee}(E_{\nu})$ were functions of E_{ν} as opposed to T_{eff} .

Appendix A explains how this parameterization can be used to describe sterile neutrino models that do not

predict any day/night asymmetry in the sterile neutrino flux and do not predict any distortion in the sterile E_ν spectrum [16]. Reference [17] presents a very general sterile neutrino analysis that includes day versus night asymmetries.

Due to the broad T_{eff} resolution of the detector, $P_{ee}^d(E_\nu)$ was not sensitive to sharp distortions and was parameterized by

$$P_{ee}^d(E_\nu) = c_0 + c_1(E_\nu[\text{MeV}] - 10) + c_2(E_\nu[\text{MeV}] - 10)^2, \quad (6)$$

where c_0 , c_1 , and c_2 were parameters defining the ν_e survival probability. Simulations showed that the fit was not sensitive to higher order terms in the polynomial. Expanding the function around 10 MeV, which corresponds approximately to the peak in the detectable ${}^8\text{B}$ neutrino E_ν spectrum, reduced correlations between c_0 , c_1 , and c_2 . For the same reasons, $A_{ee}(E_\nu)$ was parameterized by

$$A_{ee}(E_\nu) = a_0 + a_1(E_\nu[\text{MeV}] - 10), \quad (7)$$

where a_0 , and a_1 were parameters defining the relative difference between the night and day ν_e survival probability. By disallowing sharp changes in the neutrino signal that can mimic the background signal at low energies, these parameterizations reduced the covariances between the neutrino interaction and background rates.

To correctly handle ES events, we simulated ν_μ s with the same E_ν spectrum as ν_e s, such that scaling factors for these interactions in Table I were satisfied. In our previous analysis [7] we approximated the ν_μ and ν_τ cross-section by 0.156 times the ν_e cross-section, and then included an additional systematic uncertainty to account for the fact that the ratio of the ν_e to ν_μ ES cross-section is not constant as a function of E_ν .

III.2. Event selection and backgrounds

Table II summarizes the data periods used in this analysis. We used the same periods of data as our most recent analyses of data from these phases [7, 8].

TABLE II. Dates for the data in the different phases used in this analysis.

Phase	Start date	End date	Total time [days]	
			Day	Night
I	November 1999	May 2001	119.9	157.4
II	July 2001	August 2003	176.5	214.9
III	November 2004	November 2006	176.6	208.6

Event cuts to select good candidates were identical to those in the previous analyses of these data [7, 8]. The following cuts on the event variables were applied: $\rho < ({}^{550}_{[\text{cm}]} / 600_{[\text{cm}]})^3 = 0.77025$, $-0.12 < \beta_{14} < 0.95$, $3.5 \text{ MeV} < T_{\text{eff}} < 20.0 \text{ MeV}$ for Phases I and II, and $6.0 \text{ MeV} < T_{\text{eff}} < 20.0 \text{ MeV}$ for Phase III. After these

cuts the data consisted of events from ES, CC, and NC interactions of ${}^8\text{B}$ neutrinos, and a number of different background sources.

Radioactive decays produced two main background types: “electron-like” events, which resulted from β -particles or γ -rays with a total energy above our T_{eff} threshold, and neutrons produced by the photo-disintegration of deuterons by γ -rays with energies above 2.2 MeV. During Phase III, only the neutron events were observed from radioactive background decays, due to the higher T_{eff} threshold for that phase.

The radioactive decays of ${}^{214}\text{Bi}$ and ${}^{208}\text{Tl}$ within the regions of the detector filled with D_2O and H_2O were major sources of background events. ${}^{214}\text{Bi}$ is part of the ${}^{238}\text{U}$ decay chain, but it was most likely not in equilibrium with the early part of the decay chain. The most likely source of ${}^{214}\text{Bi}$ was from ${}^{222}\text{Rn}$ entering the D_2O and H_2O from mine air. ${}^{208}\text{Tl}$ is part of the ${}^{232}\text{Th}$ decay chain. These sources of radiation produced both electron-like events and photo-disintegration neutrons. *Ex-situ* measurements [18, 19] of background levels in the D_2O and H_2O provided constraints on the rate of these decays, as given in Tables XVIII and XIX of Appendix B.

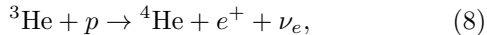
Background sources originating from the AV included decays of ${}^{208}\text{Tl}$ within the acrylic, which produced both electron-like events and photo-disintegration neutrons. In addition, radon progeny that accumulated on the surface of the AV during construction could create neutrons through (α, n) reactions on isotopes of carbon and oxygen within the AV. Near the T_{eff} threshold in Phases I and II the majority of background events originated from radioactive decays within the PMTs.

Due to the dissolved NaCl in the D_2O during Phase II, calibration sources that produced neutrons, and other sources of neutrons, led to the creation of ${}^{24}\text{Na}$ via neutron capture on ${}^{23}\text{Na}$. ${}^{24}\text{Na}$ decays with a half-life of approximately 15 hours, producing a low energy β particle and two γ -rays. One of these γ -rays has an energy of 2.75 MeV, which could photo-disintegrate a deuteron. This resulted in additional electron-like events and photo-disintegration neutrons during Phase II. Periods after calibrations were removed from the data, but there were remaining backgrounds.

During Phase III there were additional photo-disintegration neutron backgrounds due to radioactivity in the nickel and cables of the NCD array, as well as two “hotspots” on the strings referred to as K2 and K5. The estimated number of these background events, given in Table XIX of Appendix B, were based on previous analyses of these data [14] except for backgrounds from the K5 hotspot, which was based on a recent reanalysis [20]. The previously estimated number of neutrons observed in the NCD array due to the K5 hotspot was 31.6 ± 3.7 , which assumed there was Th and a small amount of U in the hotspot based on both *ex-situ* and *in-situ* measurements. Based on measurements performed on the strings after they were removed from the D_2O , it was determined that the radioactivity was likely on the surface and most

likely pure Th with very little U. This resulted in a new estimate of $45.5_{-8.4}^{+7.5}$ neutron background events observed in the NCD array from this hotspot.

Aside from the radioactive decay backgrounds, there were additional backgrounds to the ^8B neutrino measurement due to ν_e s produced by the following reaction,



in the Sun, so-called *hep* neutrinos. These have a maximum energy of 18.8 MeV, which is slightly above the ^8B neutrino maximum energy of 15 MeV, and the standard solar model (SSM) prediction for their flux is approximately one thousand times smaller than Φ_{B} [21]. Estimates of this background were based on the SSM prediction including the effects of neutrino oscillations obtained from previous analyses [7]. There were instrumental backgrounds that reconstructed near the AV. Above $T_{\text{eff}} \approx 6$ MeV these events formed a distinct peak at low values of β_{14} , so they were easily removed by the cuts on β_{14} and ρ . At lower T_{eff} , position reconstruction uncertainties increase, and the β_{14} distribution of these ‘‘AV instrumental background’’ events broadens, resulting in incomplete removal by these cuts. This background was negligible in Phase III due to the higher T_{eff} threshold used for the analysis of data from that phase. Finally, there were also background events due to neutrinos produced by particle decays in the atmosphere. The estimated numbers for these background events, given in Tables XVIII and XIX of Appendix B, were based on previous analyses of these data [7, 14].

III.3. PDFs

For Phases I and II the event variables T_{eff} , ρ , β_{14} , and $\cos\theta_{\odot}$ were used to construct 4-dimensional PDFs. For Phase III the reduced number of NC events observed with the PMT array made the β_{14} event variable unnecessary, so the PDFs were 3-dimensional in the remaining three event variables. Monte Carlo simulations were used to derive the PDFs for all signal and background classes observed with the PMT array except for backgrounds originating from radioactivity in the PMTs, which was described by an analytical function. Compared to the previous analysis of data from Phases I and II [7], we increased the number of Monte Carlo events for the CC and ES interactions by a factor of four, and for NC interactions and some background types by a factor of two.

The Monte Carlo simulation was verified using a variety of calibration sources. Based on these comparisons a number of systematic uncertainties were defined to represent possible variations in the event variables relative to the calibrations. In general these included differences in the offset, scale, and resolution for each of the event variables. Appendix B gives the complete list of systematic uncertainties associated with the PDFs. Except where specified these uncertainties were the same as those used in the most recent analyses of these data [7, 14].

Extensive calibrations using a ^{16}N γ -ray source [22], which produced electrons with kinetic energies of approximately 5.05 MeV from Compton scattering, allowed us to calibrate T_{eff} . In Phase I the linearity of T_{eff} with respect to electron kinetic energy was tested using a proton-tritium fusion γ -ray source [23], which produced electrons with kinetic energies up to approximately 19.0 MeV from Compton scattering and pair-production. Based on these sources, we parameterized the reconstructed electron kinetic energy including a possible non-linearity by

$$T_{\text{eff}}' = T_{\text{eff}} \left(1 + c_0^E \frac{T_{\text{eff}}[\text{MeV}] - 5.05}{19.0 - 5.05} \right), \quad (9)$$

where c_0^E represents the level of non-linearity. The linearity in all phases was tested using the following two electron sources: a ^8Li calibration source [24] that produced electrons with a continuous distribution up to approximately 13 MeV; and electrons with a continuous energy distribution up to approximately 50 MeV produced by the decay of muons that stopped within the AV. These studies revealed non-linearities consistent with zero. We assumed any non-linearities below our level of sensitivity were correlated between all three phases, and we used a value of $c_0^E = 0 \pm 0.0069$, which was equal to the value used in the previous analysis of data from Phases I and II [7].

During Phase III, $^{24}\text{NaCl}$ brine was injected into the D_2O on two separate occasions [25]. The brine was thoroughly mixed in the D_2O and provided a uniformly distributed source of γ -rays, allowing us to study possible T_{eff} variations in regions that were previously not sampled due to the restricted movement of the ^{16}N source. The observed variation in the event rate of ^{24}Na decays within the fiducial volume of solar neutrino analysis was consistent with what was allowed by the T_{eff} calibration parameters determined with the ^{16}N source at $T_{\text{eff}} > 6$ MeV.

While the intrinsic rate of radioactive backgrounds from solid bulk materials such as the acrylic vessel or PMT array were not expected to vary over the course of the experiment, variations in detector response make the detected rates vary over time, and because of differences in the livetime fractions between day and night, these variations were aliased into day/night differences. PDFs derived from Monte Carlo naturally include day/night detector asymmetries because the detector simulation tracks changes to the detector response. Our previous analysis derived the analytical PDFs for radioactivity originating from the PMTs using a bifurcated analysis of real data with the day and night data combined [7], which did not account for possible day/night asymmetries.

To accommodate such asymmetries in the present analysis we allowed different observed background rates between day and night, and we repeated the bifurcated analysis with the data separated into day and night sets. Similarly to the previous analysis [7] the PDF was pa-

III.4. Efficiencies

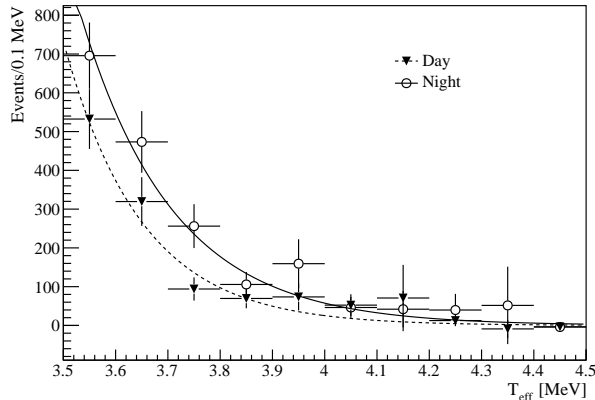


FIG. 2. T_{eff} spectra for the PMT background events obtained from a bifurcated analysis of data from Phase I including the best fits to Equation 10.

parameterized by the following function

$$P_{\text{PMT}}(T_{\text{eff}}, \beta_{14}, \rho) = e^{\epsilon T_{\text{eff}}} \times (e^{\nu \rho} + |b + 1| - 1) \times \mathcal{N}(\beta_{14}|\omega_0 + \omega_1(\rho - 0.61), \beta_s), \quad (10)$$

where ϵ , ν , b , ω_0 , ω_1 , and β_s were parameters determined from the fit to the bifurcated data. $\mathcal{N}(x|\bar{x}, \sigma)$ represents a Gaussian distribution in x with mean \bar{x} and standard deviation σ . The uncertainties in the radial parameters were obtained from one dimensional scans of the likelihood function because the magnitude operator distorted the likelihood function at $b = -1$. Compared to the function used in the previous analysis [7], $\omega_1 \rho$ was replaced with $\omega_1(\rho - 0.61)$ to reduce the correlation between ω_0 and ω_1 . Table III lists the PDF parameters from this analysis. We observed a weak day/night asymmetry in these results, in particular at roughly the 1σ level in the T_{eff} spectrum. Figure 2 shows the fits to the T_{eff} spectrum for Phase I.

TABLE III. PMT background PDF parameters as determined by a bifurcated analysis. $\rho_{\nu b}$ is the correlation between the ν and b parameters.

Parameter	Phase			
	I-day	I-night	II-day	II-night
ϵ	-6.7 ± 1.3	-5.6 ± 1.0	-6.3 ± 0.9	-7.0 ± 0.9
ν	6.6 ± 0.9	6.8 ± 1.5	5.3 ± 1.0	5.7 ± 1.1
b	-1.0 ± 1.3	3.3 ± 12.0	-0.3 ± 2.1	0.5 ± 3.0
$\rho_{\nu b}$	0.60	0.96	0.91	0.94

The E_ν spectrum of ^8B neutrinos used to derive the PDFs for ES, CC, and NC interactions was obtained, including the uncertainties, from Reference [26]. Our previous analysis of data from Phases I and II [7] included this uncertainty for the CC and ES PDFs. In this analysis we also included the effects of this uncertainty on the normalization of the NC rate.

Table XXI in Appendix B lists the uncertainties associated with neutron detection. The majority of these were identical to previous analyses of these data [7, 14] except where indicated below.

We recently published [14] an analysis based on calibration data from Phase III that determined that the fraction of neutrons created in NC interactions that were detectable with the PMT array, ϵ_n^{PMT} , was 0.0502 ± 0.0014 . The previous analysis of data from Phase III [8] used $\epsilon_n^{\text{PMT}} = 0.0485 \pm 0.0006$, which relied on a Monte Carlo based method to determine the uncertainty on the neutron detection efficiency. This new analysis avoids the dependence on Monte Carlo simulations.

Similarly, a calibration based method was used to calculate the fraction of neutrons created by NC interactions that were captured in the gas of the NCD array, ϵ_n^{NCD} . This yielded $\epsilon_n^{\text{NCD}} = 0.211 \pm 0.005$ [14], which had slightly better precision than the value of $\epsilon_n^{\text{NCD}} = 0.211 \pm 0.007$ used in the previous analysis of data from Phase III [8]. We multiplied ϵ_n^{NCD} by a correction factor of 0.862 ± 0.004 in order to determine the efficiency for detecting NC interactions in the NCD array. The correction factor, averaged over the duration of Phase III, included the mean live fraction of the signal processing systems, threshold efficiencies, and signal acceptance due to event selection cuts.

This analysis corrected a 1.2% error in the normalization of the number of NC events observed in the PMT array that was in the previous analysis of data from Phase III [8]. Because the majority of NC events were observed in the NCD array, this normalization error had a relatively small effect on the measured NC flux. In addition we have corrected a 0.1% error in the deuteron density used for that analysis.

III.5. Description of the fit

The combined fit to all phases was performed using the maximum likelihood technique, where the negative log likelihood function was minimized using MINUIT [27]. The events observed in the PMT and NCD arrays were uncorrelated, therefore the negative log likelihood function for all data was given by

$$-\log L_{\text{data}} = -\log L_{\text{PMT}} - \log L_{\text{NCD}}, \quad (11)$$

where L_{PMT} and L_{NCD} , respectively, were the likelihood functions for the events observed in the PMT and NCD arrays.

The negative log likelihood function in the PMT array

was given by

$$-\log L_{\text{PMT}} = \sum_{j=1}^N \lambda_j(\vec{\eta}) - \sum_{i=1}^{n_{\text{PMT}}} \log \left[\sum_{j=1}^N \lambda_j(\vec{\eta}) f(\vec{x}_i|j, \vec{\eta}) \right], \quad (12)$$

where N was the number of different event classes, $\vec{\eta}$ was a vector of “nuisance” parameters associated with the systematic uncertainties, $\lambda_j(\vec{\eta})$ was the mean of a Poisson distribution for the j^{th} class, \vec{x}_i was the vector of event variables for event i , n_{PMT} was the total number of events in the PMT array during the three phases, and $f(\vec{x}_i|j, \vec{\eta})$ was the PDF for events of type j .

The PDFs for the signal events were re-weighted based on Equations 6 and 7. This was a CPU intensive task that was prohibitive for the kernel based PDFs used in the previous analysis of data from Phases I and II [7]. Therefore, in that analysis, the PDFs were also binned based on E_ν , and these PDFs were then weighted by the integral of Equations 6 and 7 within that bin. This analysis did not require this approximation when calculating the best fit, although an approximation was used when “scanning” (described below) the systematic uncertainties. As described in Reference [17], $\lambda(\vec{\eta})$ was re-parameterized such that the Monte Carlo-based PDFs did not need to be normalized.

In the previous analysis of the PMT array data from Phase III [8], the nuisance parameters were only propagated on the PDFs for neutrino interactions, while this analysis also propagates these parameters on the PDFs for background events. Because the number of background events observed in the PMT array was small relative to the number of neutrino events, this had a relatively minor effect on that result.

The negative log likelihood function in the NCD array was given by

$$-\log L_{\text{NCD}} = \frac{1}{2} \left(\frac{\sum_{j=1}^N \nu_j(\vec{\eta}) - n_{\text{NCD}}}{\sigma_{\text{NCD}}} \right)^2, \quad (13)$$

where $\nu_j(\vec{\eta})$ was the mean of a Poisson distribution for the j^{th} class, n_{NCD} was the total number of neutrons observed in the NCD array based on the fit described in Section IV.2, and σ_{NCD} was the associated uncertainty.

The mean number of events for a given class was often related to the mean number of events for another class; for instance, the number of ES, CC, and NC events in each phase were determined from the parameters in Section III.1.

Constraints were placed on various nuisance parameters and the rate of certain classes of background events. Including these constraints, the negative log likelihood function was given by

$$-\log L = -\log L_{\text{data}} + \frac{1}{2}(\vec{\eta} - \vec{\mu})^T \Sigma^{-1}(\vec{\eta} - \vec{\mu}), \quad (14)$$

where $\vec{\eta}$ was the value of the nuisance parameters, $\vec{\mu}$ was the constraint on the parameters, and Σ was the covariance matrix for the constraints. Appendix B lists all of the constraints.

Our previous analysis of data from Phases I and II [7] imposed a physical bound on background rates, so that they were not allowed to become negative in the fit. Without these bounds the background from neutrons originating from the AV in Phase II favors a rate whose central value was negative, but consistent with zero. The uncertainty in the PDFs due to the finite Monte Carlo statistics could explain the fitted negative value. The previously reported ensemble tests [7] used a central value for this background that was more than two statistical standard deviations above zero, such that no significant effect from the bound was observed. Using a positive bound for the backgrounds when ensemble testing with Monte Carlo data that does not contain any neutrons originating from the AV in Phase II tends to shift Φ_B down on average compared to the flux used to simulate the data, as we only obtained background rates that were equal to or higher than the values used in the simulations. Removing this bound allowed closer agreement between the expectation values for the signal parameters and the values used in the simulated data. We therefore removed these bounds in this analysis to provide a more frequentist approach that facilitates the combination of the SNO results with other experiments.

In the previous analysis of data from Phases I and II [7] the background constraints obtained for the average of the day and night rate (e.g. for the *ex-situ* measurements of ^{214}Bi and ^{208}Tl) were applied independently to both the day and the night rates, which resulted in a narrower constraint on these backgrounds than we intended. This analysis correctly applies this as a day and night averaged constraint.

Because of the large number of constraints, and the time involved in modifying some PDFs, there were three methods for handling the nuisance parameters. Some were “floated,” i.e. allowed to vary within the MINUIT minimization of the negative log likelihood function. Others were “scanned,” where a series of fits were performed with different values of the parameter in order to find the best fit. This process was repeated for all scanned nuisance parameters multiple times to converge on the global minimum of the fit. Finally, some were “shifted-and-refitted,” where the central values of the fit parameters were not varied, but the effect of the nuisance parameter on the uncertainties was calculated. The method used for each parameter depended on the size of that constraints effect on Φ_B and the ν_e survival probability parameters. Appendix B lists how each nuisance parameter was treated.

In addition to the systematic uncertainties considered in previous analyses, this analysis also included a systematic uncertainty due to the finite Monte Carlo statistics used to construct the PDFs. We performed 1000 independent fits in which the number of events in each bin of

the PDF were drawn from a Poisson distribution. The uncertainty due to the finite Monte Carlo statistics was determined from the distribution of the fit parameters.

In order to calculate the total systematic uncertainty on the Φ_B and the ν_e survival probability parameters, we applied the shift-and-refit 100 times for each parameter in order to calculate the asymmetrical likelihood distribution for that parameter. We then performed one million fits with the nuisance parameters drawn randomly from these distributions. The total systematic uncertainty was obtained from the resulting distribution of the fit results. This is the first time we have applied this procedure, which correctly accounts for the combination of asymmetrical uncertainties. In order to calculate the effects of the day/night or MC systematic uncertainties, respectively, this procedure was repeated with only the nuisance parameter related to day/night differences or MC statistics varied.

In total the fit included Φ_B , the five ν_e survival probability parameters described in Section III.1, 36 background rate parameters, 35 floated or scanned nuisance parameters, and 82 shift-and-refit nuisance parameters.

The biases and uncertainties obtained from this analysis method were tested using simulated data. The number of simulated sets of data was restricted by the amount of Monte Carlo data available. For simulated data containing neutrino interactions and some background classes, we did bias tests with 250 sets of data. For simulated data containing neutrino interactions and all background classes, we did bias tests with 14 sets of data. All of these tests showed the method was unbiased and produced uncertainties consistent with frequentist statistics.

III.6. Crosschecks

As a crosscheck on the analysis method described above, we developed two independent analyses. The first crosscheck compared the results from the above method run only on data from Phases I and II. This was cross-checked against the method described in the previous analysis of this data [7] with the most significant changes from this analysis included in that previous analysis. The results from the two methods were in agreement.

We developed an alternate Bayesian based analysis where the posterior probability distribution was sampled using a Markov Chain Monte Carlo (MCMC). This analysis was applied to data from Phase III, using the results from the maximum likelihood analysis performed on data from Phases I and II as a prior. The priors for background and neutrino interaction rates had zero probability for negative rates and were uniform for positive rates. There were two important differences between this alternate analysis and the maximum likelihood method described above. Firstly, because the systematic uncertainties were varied in each step of the MCMC, the uncertainties included all systematic and statistical uncer-

ainties. Secondly, this method samples the entire posterior probability distribution instead of identifying the maximum likelihood. Reference [28] provides details of this method. As shown in Section V the results of the Bayesian and maximum likelihood fits agreed. An alternate Bayesian analysis was also performed with details provided in Reference [29]. Though this analysis was not used as a direct crosscheck, its results were consistent with the analysis presented here.

IV. NCD ARRAY ANALYSIS

The NCD array observed neutrons, alphas, and events caused by instrumental backgrounds. Because of their low stopping power in the gas of the proportional counters, electrons rarely triggered the NCD array. A series of cuts described in Reference [14] removed the instrumental backgrounds. For neutron events E_{NCD} was peaked at approximately 0.76 MeV, with a maximum energy of 0.85 MeV when including the resolution. E_{NCD} was less than 0.76 MeV if the proton or triton hit the nickel walls before losing all their energy. We identified the following two major categories of alpha events: so-called bulk alphas, which came from radioactive decays occurring throughout the nickel bodies of the proportional counters due to the presence of U and Th and their progeny, and so-called surface alphas, coming from the decay of ^{210}Po , which was supported by ^{210}Pb that had plated onto the inner surface of the nickel bodies. Below 1.4 MeV both types of alpha events produced relatively flat E_{NCD} spectra. Due to differences in construction of the strings, the number of alpha events varied from string-to-string.

The previous analysis of data from Phase III [8] distinguished between neutron and alpha events by fitting the E_{NCD} spectrum. The PDF of E_{NCD} for neutron events was obtained from calibration data, and for alpha events it was obtained from simulations. Between 0.4 MeV and 1.4 MeV the fitted number of alpha and neutron events, respectively, were approximately 5560 and 1170. The large number of alpha events resulted in both a large statistical uncertainty, and a large systematic uncertainty due to difficulties in accurately determining the PDF of E_{NCD} for alpha events.

The waveforms of neutron events could be significantly broader than those from alpha events, depending on the orientation of the proton-triton trajectory. This distinction was lessened by the significant tail in the waveforms caused by the long ion drift times. In an attempt to reduce the number of alpha events, and therefore the uncertainties associated with them, we developed four different particle identification (PID) parameters and a cut on these parameters. As described Section IV.1, this cut reduced the number of events in the strings filled with ^4He (alpha events) by more than 98%, while maintaining 74.78% of the neutron events. Section IV.2 describes the fit to the E_{NCD} spectrum after this cut.

These analyses rely heavily on two calibration peri-

ods with a ^{24}Na source distributed uniformly throughout the detector [25], which produced neutrons similar to those from ^8B neutrino NC reactions. These calibrations were performed in 2005 and 2006, and were respectively referred to as ^{24}Na -2005 and ^{24}Na -2006. A composite source of ^{241}Am and ^9Be , referred to as AmBe, produced a point-like source of neutrons. This source was positioned throughout the detector during six significant calibration campaigns spanning Phase III. These data were useful for assessing systematic uncertainties associated with temporal and spatial variations in the neutron detection efficiency and PDF of E_{NCD} .

IV.1. Particle identification in the NCD array

Before analyzing the waveforms, the effect of the logarithmic amplifier was removed using parameters determined from various calibration pulses in a process referred to as de-logging [14].

Two particle identification parameters, p_a and p_b , were based on fitting the waveforms to libraries of known neutron and alpha waveforms. Each waveform was fitted to each library waveform based on a χ^2 method. The relative start time of the event and library waveforms was varied to find the minimum χ^2 . In both cases the fits did not extend to later times to avoid the effects of ion mobility. Both of these particle identification parameters were defined by

$$\log \left(\frac{\chi_\alpha^2}{\chi_n^2} \right), \quad (15)$$

where χ_α^2 and χ_n^2 , respectively, were the best χ^2 s from the alpha and neutron hypotheses. The libraries used to calculate p_a were primarily based on simulation [30], and the χ^2 was calculated between where the waveform first crossed a value equal to 10% of the peak value and where it first returned to 30% of the peak value [31]. Figure 3 shows some sample fits. This clearly shows the broad waveform for neutrons with a proton-triton trajectory that was roughly perpendicular to the anode, which allows them to be separated from alphas.

To calculate p_b , the neutron library was obtained from ^{24}Na -2005 data, and the alpha library was obtained from events on the strings filled with ^4He [32]. The χ^2 was calculated between where the waveform first crossed a value equal to 10% of the peak value and where it first returned to 40% of the peak value. The libraries for this parameter included events that were used in later studies to evaluate performance. We excluded fitting a waveform to itself because this would result in a χ^2 equal to zero, i.e. a perfect match.

The remaining two particle identification parameters, p_c and p_d , were respectively based on the kurtosis and skewness of the waveform after smoothing the waveform and deconvolving the effects of ion mobility assuming an ion drift time of 16 ns. The skewness and kurtosis were calculated using the region between where the waveform

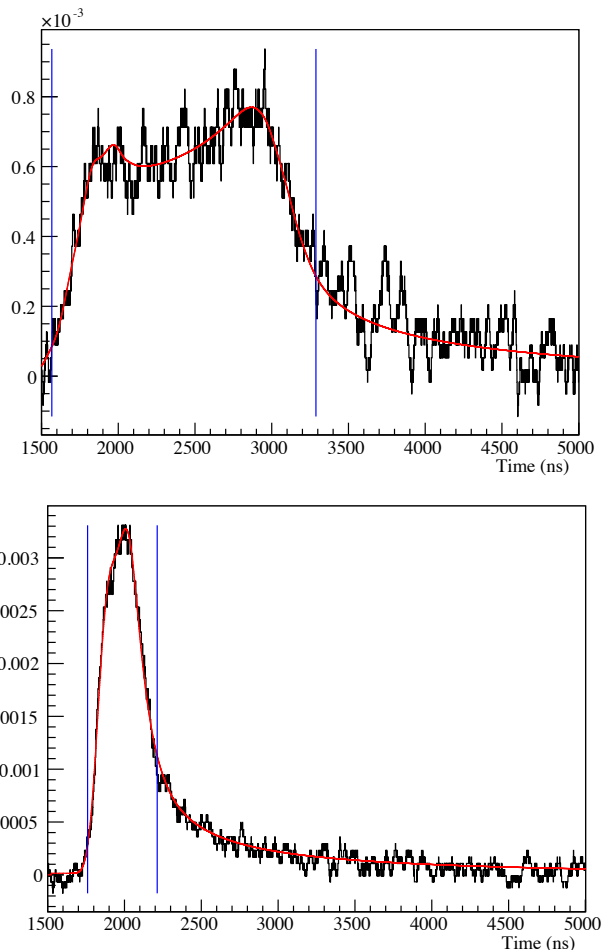


FIG. 3. Sample waveforms. The top plot shows a neutron waveform (black) obtained from ^{24}Na calibration data with the best fit to the neutron hypothesis (red). The bottom plot shows an alpha waveform (black) obtained from a string filled with ^4He with the best fit to the alpha hypothesis (red). The vertical lines represent the fit boundaries.

first crossed a value equal to 20% of the maximum and where it first returned to 20% of the peak value.

Figure 4 shows the distribution of the particle identification parameters for known neutron and alpha events. The left plot shows that p_a and p_b were highly correlated, which was unsurprising given their similar definitions. This plot also shows that a cut on these two parameters (PID cut 1) removes almost all alpha events while preserving the majority of neutron events. This cut selected events where the alpha hypothesis was significantly worse than the neutron hypothesis. After this cut, we recovered approximately 5% of the neutron events with a second cut on p_c and p_d (PID cut 2). PID cut 2 was only applied to events that failed PID cut 1, and selected events with high skewness (p_d) or low kurtosis (p_c), i.e. the waveforms were not symmetric in time or had a relatively flat peak. This combined cut, selecting events that passed PID cuts 1 or 2, was used for the rest

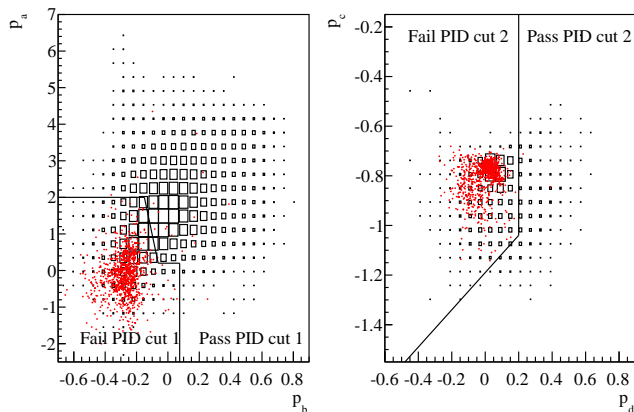


FIG. 4. Distribution of particle identification parameters for neutron events (boxes, where the area represents the number of events) and alpha events (red marks). The line represents the boundary for cuts. PID cut 1 applies to parameters p_a and p_b , and PID cut 2 applies to parameters p_c and p_d for events that failed PID cut 1.

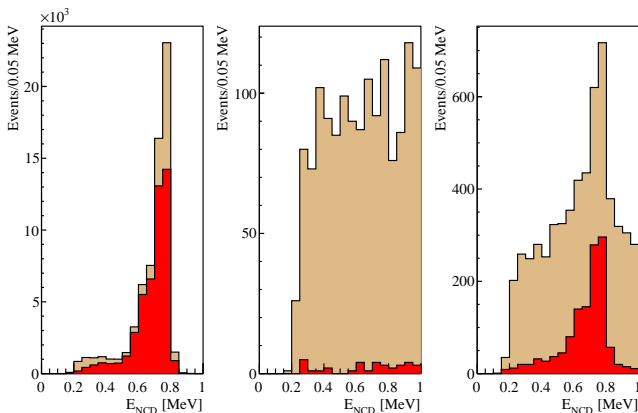


FIG. 5. E_{NCD} spectrum before (brown) and after (red) the particle identification cut. From left to right the plots are for ^{24}Na calibration data (neutrons), data from strings filled with ^4He (alphas), and data from strings filled with ^3He .

of this analysis.

Figure 5 shows that the particle identification cut removes almost all the events on the strings filled with ^4He , i.e. alpha events, while maintaining the majority of the ^{24}Na calibration events, i.e. neutron events. This also shows that the fraction of alpha events removed by the particle identification cut was relatively constant as a function of E_{NCD} . The right most plot of Figure 5 shows that the alpha background was significantly reduced, leaving what was clearly mostly neutron events.

Figure 6 shows the fraction of neutron events surviving the combined particle identification cut, ϵ_{PID} , as a function of neutron capture string for ^{24}Na -2005 and ^{24}Na -

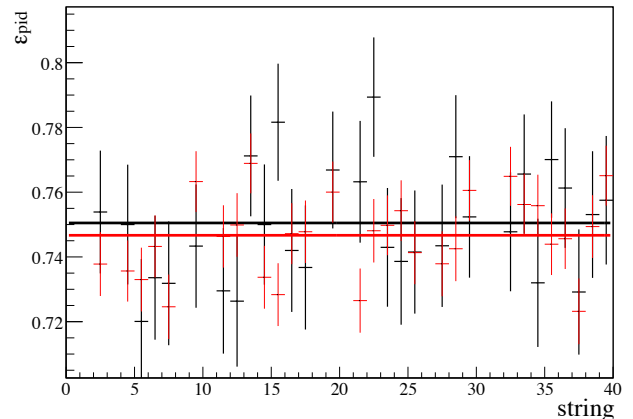


FIG. 6. ϵ_{PID} as a function of string for the ^{24}Na -2005 (black) and ^{24}Na -2006 (red) data. Fits to straight lines give 0.7505 ± 0.0035 with χ^2/NDF of 24.1/29 and 0.7467 ± 0.0018 with χ^2/NDF of 49.3/29, respectively.

2006 data. Table IV shows the average obtained from these measurements. The high χ^2/NDF obtained with the ^{24}Na -2006 data suggests a slight variation in ϵ_{PID} as a function of string; however, the correlation between the ϵ_{PID} calculated for each string between the 2005 and 2006 calibrations was only 0.159, which was so small that it suggested random string-to-string variation instead of a feature of the NCD array.

TABLE IV. ϵ_{PID} obtained with the ^{24}Na -2005 and ^{24}Na -2006 data. The weighted average included a scaling of the uncertainty by $\sqrt{\chi^2/\text{NDF}}$ for the ^{24}Na -2006 data.

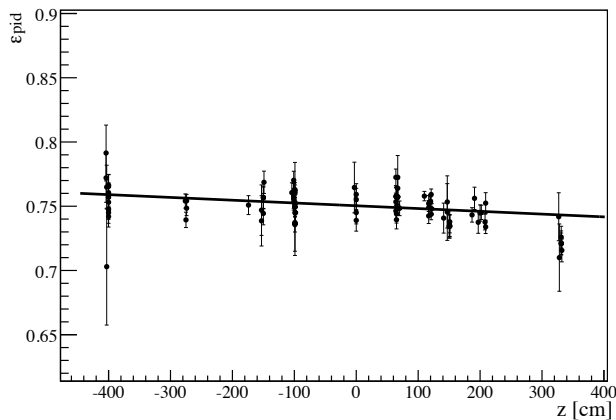
Data	ϵ_{PID}	χ^2/NDF
^{24}Na -2005	0.7505 ± 0.0035	24.1/29
^{24}Na -2006	0.7467 ± 0.0018	49.3/29
Weighted average	0.7478 ± 0.0019	

Table V summarizes the systematic uncertainties associated with ϵ_{PID} . Based on the methods for deriving these systematic uncertainties, we assumed most correlations were zero. A correlation of 0.50 was assumed between the following pairs of systematic uncertainties: de-logging and ^{24}Na uniformity, de-logging and temporal variation, p_a correction and ^{24}Na uniformity, p_a correction and temporal variation, and p_a correction and de-logging. Including these correlations the total absolute systematic uncertainty was 0.0065. Combining the systematic and statistical uncertainties in quadrature led to a total absolute uncertainty of 0.0068.

The ^{24}Na calibration data used to calculate ϵ_{PID} had a measured variation in the neutron production rate as a function of z position of less than 10% between the maximum and the value at $z = 0$. Figure 7 shows that

TABLE V. Absolute systematic uncertainties for ϵ_{PID} .

Systematic uncertainty	
^{24}Na uniformity	0.0010
Temporal variation	0.0037
Contamination	0.0019
De-logging	0.0018
p_a correction	0.0010
p_b neutron library	0.0019
Total	0.0065

FIG. 7. ϵ_{PID} as function of z for a single string. This was typical of all strings.

the dependence of ϵ_{PID} with source position, as measured with the AmBe data, was well approximated by a linear function with a maximum deviation compared to that at $z = 0$ of less than 0.01. Combining the possible non-uniformity in the ^{24}Na source distribution with the variation in ϵ_{PID} as a function of z position resulted in an absolute systematic uncertainty in ϵ_{PID} due to ^{24}Na uniformity of 0.0010. The variation due to the x and y position non-uniformity was accounted for in the string averaging used to calculate ϵ_{PID} .

The systematic uncertainty in ϵ_{PID} due to temporal variations was estimated based on the standard deviation of ϵ_{PID} calculated from the AmBe data averaged over all strings, and calculated at $z = 0$ assuming a linear dependence on z . The systematic uncertainty in ϵ_{PID} due to alpha events contaminating the ^{24}Na calibrations was estimated using the number of events with E_{NCD} between 0.9 MeV and 1.4 MeV as an estimate of the alpha contamination. The systematic uncertainty in ϵ_{PID} due to the de-logging process was estimated by recalculating ϵ_{PID} with the individual de-logging parameters shifted by their estimated uncertainties; because of possible correlations, the magnitude of the maximum shifts with each parameter were added together.

A correction to the p_a parameter based on ^{24}Na and AmBe data reduced the spatial and temporal variations

in this parameter. A systematic uncertainty to account for the effect of this correction was estimated by calculating ϵ_{PID} assuming a one standard deviation shift in the correction to the p_a parameter and then combining the shifts caused by each string in quadrature, which assumed that the corrections from string-to-string were not correlated.

The ^{24}Na -2005 data were used in both the neutron library used to calculate p_b , and in the determination of ϵ_{PID} . Although we did not expect this to bias the calculation of ϵ_{PID} , we conservatively included an additional absolute uncertainty of 0.0019, half the difference between ϵ_{PID} calculated with the ^{24}Na -2005 and ^{24}Na -2006 data.

IV.2. Method for fitting the NCD array data

After the particle identification cut, the number of neutron events was determined from a likelihood fit to a histogram of E_{NCD} with 50 bins uniformly spaced between 0.4 and 0.9 MeV.

The PDF of E_{NCD} for neutron events was obtained from ^{24}Na -2006 data, and for alpha events it was approximated by

$$P_\alpha(E_{\text{NCD}}) = p_0 \left[P_0(E_{\text{NCD}}) + \sum_{n=1}^{N_{\text{max}}} p_n P_n(E_{\text{NCD}}) \right], \quad (16)$$

where p_0 and the p_n s were fit parameters, $P_n(E_{\text{NCD}})$ is the Legendre polynomial of order n : $P_0 = 1$, $P_1 = x$, $P_2 = 1/2(3x^2 - 1)$, $P_3 = 1/2(5x^3 - 3x)$, $P_4 = 1/8(35x^4 - 30x^2 + 3)$, with $x = 4(E_{\text{NCD}}[\text{MeV}] - 0.65)$. In order to ensure a well defined PDF, negative values of this function were set to zero. The fit was repeated with different values for the systematic uncertainties associated with the E_{NCD} scale, a_1^{NCDE} , and resolution, b_0^{NCDE} , (see Equation B18 in Appendix B) selected from a 2-dimension scan of these parameters. The point in this 2-dimensional scan with the minimum χ^2 was chosen as the best fit point, and the systematic uncertainty associated with a_1^{NCDE} and b_0^{NCDE} was obtained from the maximum difference in the number of neutron events from the best fit point at the 1σ contour.

This fit was performed for values of N_{max} up to four, at which point, based on simulations, the polynomial started to fit to fluctuations in the data. We started with the assumption that a zeroth order polynomial was a satisfactory fit to the alpha background. If a higher order polynomial had a significant improvement in χ^2 then this became the new default, and this was tested against higher order polynomials. A significant improvement in χ^2 was defined as a decrease in χ^2 that would result in a 32% probability for accepting the higher order polynomial when the higher order was not a better model. This calculation included the fact that testing against many different higher order polynomials increases

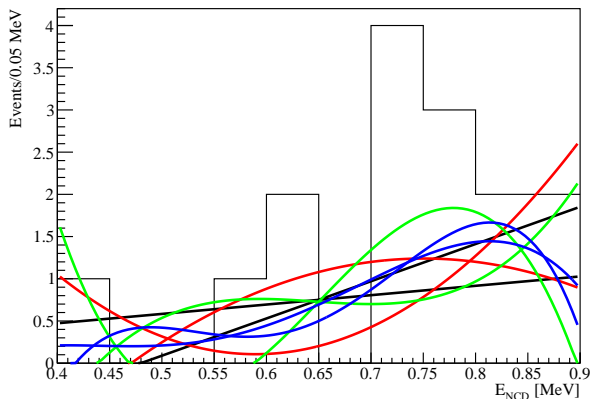


FIG. 8. E_{NCD} spectrum for events on the strings filled with ${}^4\text{He}$ after the particle identification cut. The black, red, green, and blue lines, respectively, show the PDFs used to simulate alpha events for N_{max} equal to one, two, three, and four.

the chances of erroneously choosing a higher order polynomial, so a larger improvement in χ^2 was required. Reference [33] gives the changes in χ^2 defined as significant. This method was generic to any type of background, including instrumental backgrounds, provided they did not have features sharper than the assumed background shape.

We tested the bias of this method using simulated data. The mean number of neutron events in these sets of simulated data was based on the number of neutrons obtained from the previous analysis of data from Phase III [8] and ϵ_{PID} . The E_{NCD} values for these simulated neutron events were obtained from events that passed the particle identification cut in the ${}^{24}\text{Na}$ -2006 data [34]. The mean number of alpha events in these sets of simulated data was based on the number of alphas obtained from the previous analysis of data from Phase III [8] and the approximate fraction of alpha events removed by the particle identification cut. The E_{NCD} values for the simulated alpha events were obtained from events that passed the particle identification cut in the strings filled with ${}^4\text{He}$. Because these strings did not have enough events, instead of using these events directly, we fitted the limited data to polynomials of the form in Equation 16 with N_{max} varied from 1 to 4, and then used these polynomials to simulate as many E_{NCD} values as necessary. In order to test extreme possibilities for the alpha event E_{NCD} distributions, the highest order term from the fit was changed by plus and minus 2σ , resulting in the eight different PDFs shown in Figure 8. The bias was less than 2% for all eight alpha PDFs.

Since only the ${}^{24}\text{Na}$ -2006 data were used to determine the PDF of E_{NCD} for neutrons, we included additional systematic uncertainties to account for changes in this PDF due to non-uniformity of the ${}^{24}\text{Na}$ source and possible temporal variations. The size of these systematic un-

certainties were estimated using AmBe calibration data collected at various positions and times to calculate the PDF of E_{NCD} for neutron events, and then calculating the size of the shift in the reconstructed number of neutron events. The systematic uncertainties from the temporal and position variation were summed in quadrature to give a total systematic uncertainty of 0.64% on the number of neutrons obtained from the fit due to the PDF of E_{NCD} for neutron events.

V. RESULTS

Section V.1 presents the results from the analysis of data from the NCD array in Phase III. Because this was a new analysis of this data, we used a statistically-limited and randomly-selected one-third subset of the data to develop the particle identification cut and analysis. Once we had finalized all aspects of this analysis we fitted the entire set of data from the NCD array in Phase III. After completing this full analysis we realized that there was an error in the method to calculate the systematic uncertainty due to a_1^{NCDE} and b_0^{NCDE} , which was corrected in the results presented here.

The total number of neutron events detected in the NCD array obtained from this new analysis of data from Phase III was then used as a constraint in the fits to the combined data presented in Section V.2. The combined analysis of the three phases also used a statistically-limited and randomly-selected one-third subset of the data to develop the fitting method. Once we had finalized all aspects of this analysis we fitted the entire set of data from all three phases.

V.1. Results from fit to NCD array data

Table VI shows the χ^2 and statistical uncertainty from the fit to the E_{NCD} spectrum for various values of N_{max} in Equation 16. In general including extra terms in the PDF of E_{NCD} for alpha events should not result in best fits with higher χ^2 , but this can occur if the minimization routine finds different local minima. Based on our method for choosing the value of N_{max} representing the point where improvements in fit quality cease, the best fit occurs when $N_{\text{max}} = 4$. This corresponded to the maximum value of N_{max} considered before performing the fit, so to check that larger values of N_{max} did not produce better fits, we also fitted with N_{max} equal to five and six, as shown in Table VI. These fits did not produce better results.

Figure 9 shows the best fit of the E_{NCD} spectrum. Although the best fit turns down at higher values of E_{NCD} the parameters were consistent with a flat PDF in that region. This variation in the allowed PDF was reflected in the increased statistical uncertainty with large N_{max} .

For the fit with $N_{\text{max}} = 4$ the systematic uncertainty due to a_1^{NCDE} and b_0^{NCDE} was 5 neutrons. Combining this

TABLE VI. χ^2 and 1σ statistical uncertainty for various values of N_{\max} in Equation 16.

N_{\max}	χ^2/NDF	Stat. uncertainty
0	54.92/48	4.2%
1	56.72/47	4.2%
2	47.63/46	5.5%
3	41.78/45	6.5%
4	40.20/44	6.9%
5	40.34/43	9.4%
6	40.41/42	9.2%

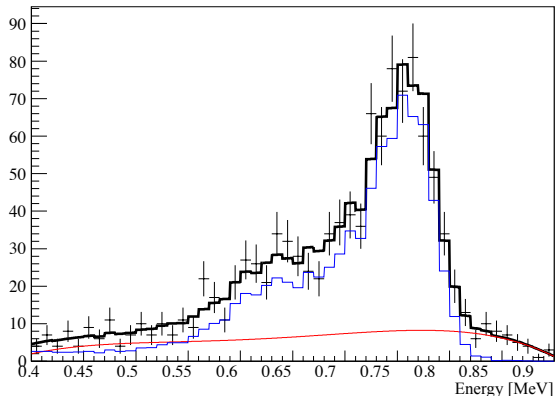


FIG. 9. The fitted E_{NCD} spectrum after the particle identification cut. The thick black line is the best fit. The blue and red lines are the best fitted neutron and alpha spectra, respectively.

with the systematic uncertainty in the PDF of E_{NCD} for neutrons, the statistical uncertainty in the fit, and dividing by ϵ_{PID} , the total number of neutrons observed in the NCD array equals 1115 ± 79 . The previous analysis of data from Phase III gave 1168 neutrons in the NCD array, with similar uncertainty [8]. That analysis had a large background due to alpha events, which made the assessment of the systematic uncertainty on the fitted number of events more challenging. The result presented here avoids that problem by eliminating most of the background from alpha events and allowing a very general PDF to describe the E_{NCD} spectrum for any remaining background events. Since the particle identification cut removed almost all alpha events, the fitted number of neutron events had a small to moderate correlation with the previous analysis of this data.

V.2. Results from combined fit to all data

For the combined fit to all data using the maximum likelihood technique, Table VII shows Φ_{B} and the ν_e survival probability parameters as defined in Equations 6 and 7 of Section III.1. Table VIII shows the

correlation between these parameters. The combined fit to all data from SNO yielded a total flux of active neutrino flavors from ${}^8\text{B}$ decays in the Sun of $\Phi_{\text{B}} = (5.25 \pm 0.16(\text{stat.})^{+0.11}(\text{syst.})_{-0.13}) \times 10^6 \text{ cm}^{-2}\text{s}^{-1}$. During the day the ν_e survival probability at 10 MeV was $c_0 = 0.317 \pm 0.016(\text{stat.}) \pm 0.009(\text{syst.})$, which was inconsistent with the null hypothesis that there were no neutrino oscillations at very high significance. Using the covariance matrix obtained from this combined analysis we can compare the best fit to various null hypotheses. The null hypothesis that there were no spectral distortions of the ν_e survival probability (i.e. $c_1 = 0, c_2 = 0, a_0 = 0, a_1 = 0$), yielded $\Delta\chi^2 = 1.97$ (26% C.L.) compared to the best fit. The null hypothesis that there were no day/night distortions of the ν_e survival probability (i.e. $a_0 = 0, a_1 = 0$), yielded $\Delta\chi^2 = 1.87$ (61% C.L.) compared to the best fit.

TABLE VII. Results from the maximum likelihood fit. Note that Φ_{B} is in units of $\times 10^6 \text{ cm}^{-2}\text{s}^{-1}$. The D/N systematic uncertainties includes the effect of all nuisance parameters that were applied differently between day and night. The MC systematic uncertainties includes the effect of varying the number of events in the Monte Carlo based on Poisson statistics. The basic systematic uncertainties include the effects of all other nuisance parameters.

	Best fit	Stat.	Systematic uncertainty			
			Basic	D/N	MC	Total
Φ_{B}	5.25	± 0.16	$+0.11$ -0.12	± 0.01	$+0.01$ -0.03	$+0.11$ -0.13
c_0	0.317	± 0.016	$+0.008$ -0.010	± 0.002	$+0.002$ -0.001	± 0.009
c_1	0.0039	$+0.0065$ -0.0067	$+0.0047$ -0.0038	$+0.0012$ -0.0018	$+0.0004$ -0.0008	± 0.0045
c_2	-0.0010 ± 0.0029	$+0.0013$ -0.0016	$+0.0002$ -0.0003	$+0.0004$ -0.0002	$+0.0004$ -0.0002	$+0.0014$ -0.0016
a_0	0.046	± 0.031	$+0.007$ -0.005	± 0.012	$+0.002$ -0.003	$+0.014$ -0.013
a_1	-0.016	± 0.025	$+0.003$ -0.006	± 0.009	± 0.002	$+0.010$ -0.011

TABLE VIII. Correlation matrix from the maximum likelihood fit.

	Φ_{B}	c_0	c_1	c_2	a_0	a_1
Φ_{B}	1.000	-0.723	0.302	-0.168	0.028	-0.012
c_0	-0.723	1.000	-0.299	-0.366	-0.376	0.129
c_1	0.302	-0.299	1.000	-0.206	0.219	-0.677
c_2	-0.168	-0.366	-0.206	1.000	0.008	-0.035
a_0	0.028	-0.376	0.219	0.008	1.000	-0.297
a_1	-0.012	0.129	-0.677	-0.035	-0.297	1.000

Figure 10 shows the RMS spread in $P_{ee}^{\text{d}}(E_{\nu})$ and $A_{ee}(E_{\nu})$, taking into account the parameter uncertainties and correlations. This also shows that the maximum likelihood analysis was consistent with the alternative Bayesian analysis. Reference [35] contains all steps of the MCMC fit after the fit had converged.

Figures 11, 12, and 13, respectively, show one-dimensional projections of the fit for Phase I, II, and III.

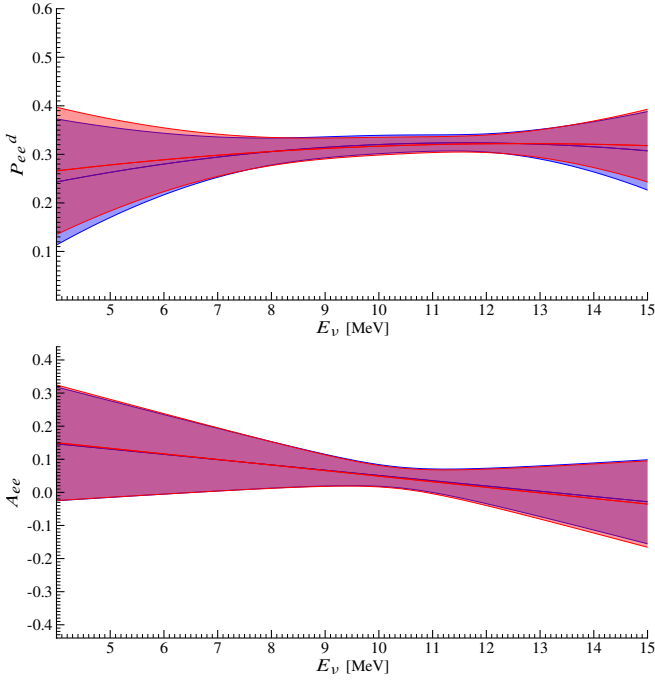


FIG. 10. RMS spread in $P_{ee}^d(E_\nu)$ and $A_{ee}(E_\nu)$, taking into account the parameter uncertainties and correlations. The red band represents the results from the maximum likelihood fit, and the blue band represents the results from the Bayesian fit. The red and blue solid lines, respectively, are the best fits from the maximum likelihood and Bayesian fits.

VI. NEUTRINO OSCILLATIONS

Solar models predict the fluxes of neutrinos at the Earth, but the flavors of those neutrinos depends on the neutrino oscillation parameters and the details of where the neutrinos were produced in the Sun. Section VI.1 describes how the flavor components of the neutrino fluxes were calculated, and Section VI.2 describes how these predictions were compared to results for Φ_B , $P_{ee}^d(E_\nu)$, and $A_{ee}(E_\nu)$ presented here, and with other solar neutrino experiments. Reference [36] provides further details on the neutrino oscillation analysis presented here.

We considered two different neutrino oscillation hypotheses in this analysis. For comparison with previous SNO analyses, Section VI.3 presents the so-called two-flavor neutrino oscillations, which assumed $\theta_{13} = 0$ and had two free neutrino oscillation parameters, θ_{12} , and Δm_{21}^2 . In Section VI.4 we also considered the so-called three-flavor neutrino oscillations, which had the following three free neutrino oscillation parameters: θ_{12} , θ_{13} , and Δm_{21}^2 . Note that the mixing angle, θ_{23} , and the CP-violating phase, δ , are irrelevant for the neutrino oscillation analysis of solar neutrino data. The solar neutrino data considered here was insensitive to the exact value Δm_{31}^2 , so we used a fixed value of $\pm 2.45 \times 10^3 \text{ eV}^2$ obtained from long-baseline accelerator experiments and atmospheric neutrino experiments [37].

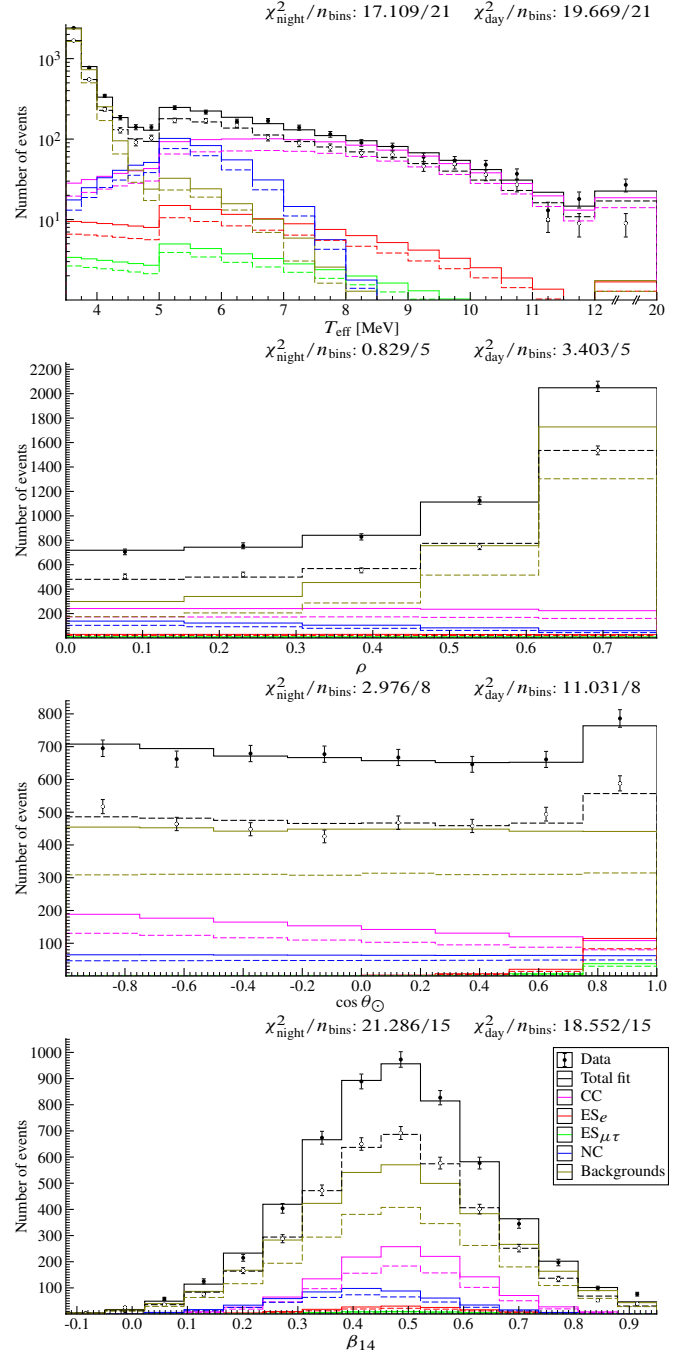


FIG. 11. Projection of the T_{eff} , ρ , $\cos\theta_\odot$, and β_{14} for the Phase I data. Day events hollow circles and dashed lines. Night events filled circle and solid lines. Note that the sharp break in the data in the top panel at 5 MeV arises from change of bin width.

VI.1. Solar neutrino predictions

Predicting the solar neutrino flux and E_ν spectrum for all neutrino flavors requires a model of the neutrino production rates as a function of location within the Sun, and a model of the neutrino survival probabili-

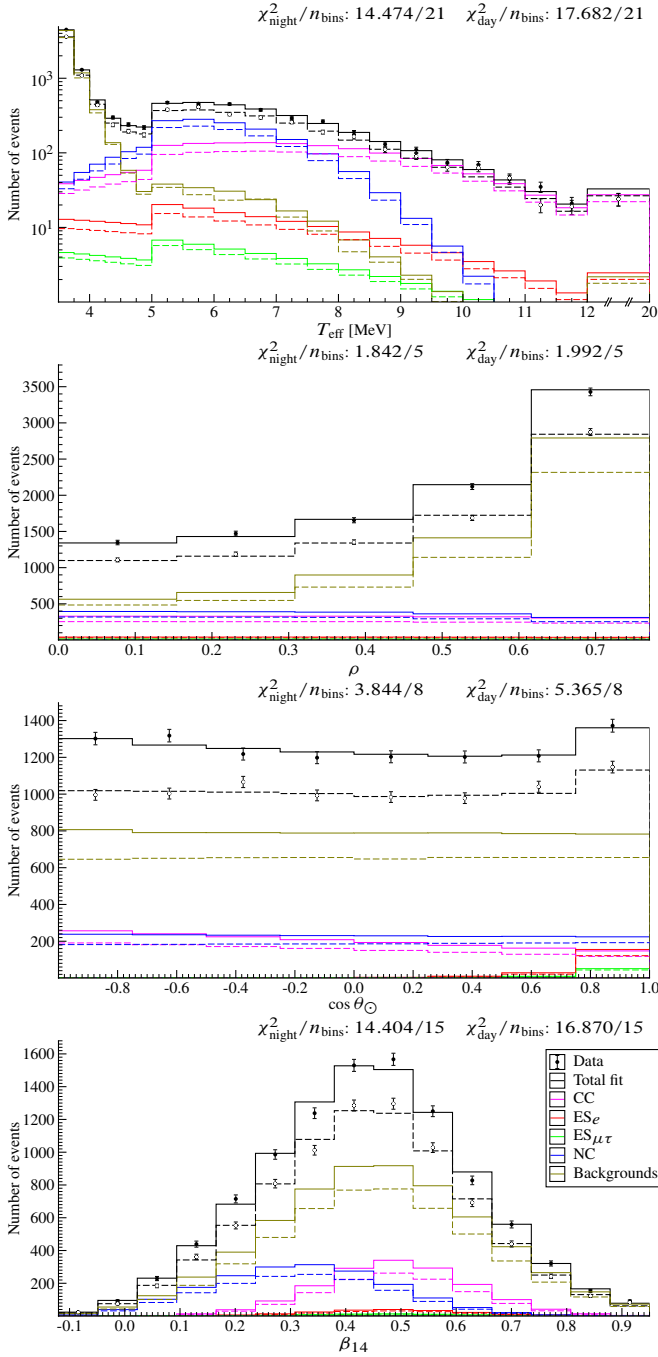


FIG. 12. Projection of the T_{eff} , ρ , $\cos\theta_{\odot}$, and β_{14} for the Phase II data. Day events hollow circles and dashed lines. Night events filled circle and solid lines. Note that the sharp break in the data in the top panel at 5 MeV arises from change of bin width.

ties as they propagate through the Sun, travel to the Earth, and then propagate through the Earth. For consistency with previous calculations, and because of the conservative model uncertainties, we used the BS05(OP) model [21] to predict the solar neutrino production rate within the Sun rather than the more recent BPS09(GS) or BPS09(AGSS09) models [6]. Reference [35] provides

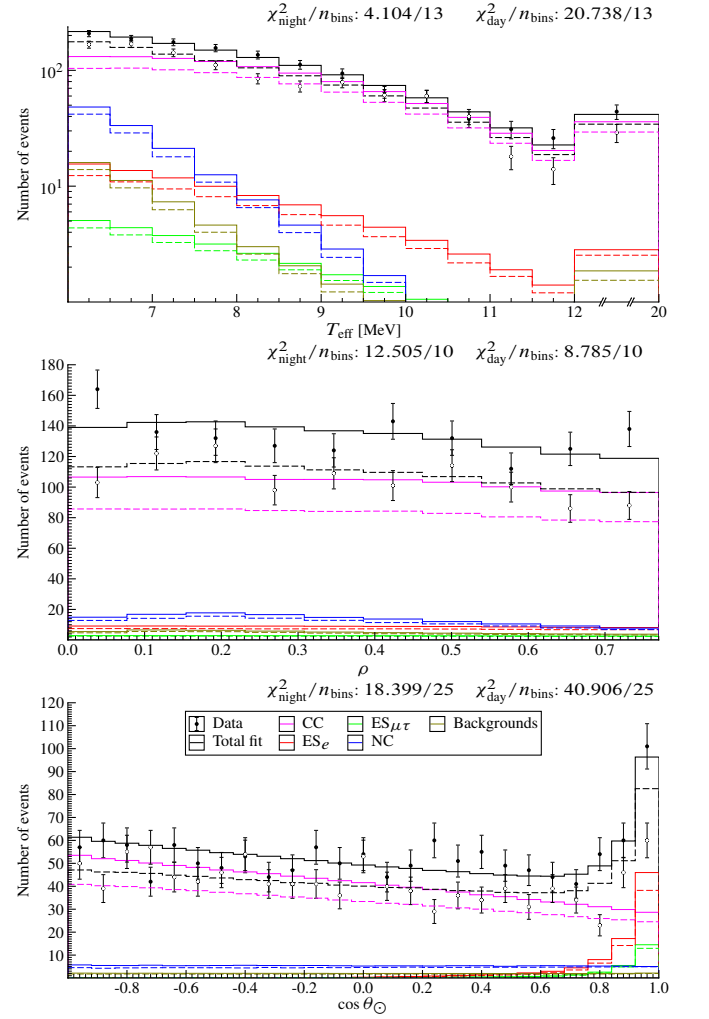


FIG. 13. Projection of the T_{eff} , ρ , and $\cos\theta_{\odot}$ for the data from Phase III. Day events hollow circles and dashed lines. Night events filled circle and solid lines.

the results presented below assuming these other solar models. We used the E_{ν} spectrum for ${}^8\text{B}$ neutrinos from Reference [26], and all other spectra were from Reference [38].

In previous analyses we used numerical calculations to construct a lookup table of neutrino survival probability as a function of the neutrino oscillation parameters. Such a table was still used to study the entire region of neutrino oscillation parameters. Previous analyses of SNO data combined with other solar neutrino experiments left only the region referred to as LMA. This analysis used an adiabatic approximation when calculating neutrino oscillation parameters in that region. We verified that these two calculations gave equivalent results for a fixed set of neutrino oscillation parameters in the LMA region. Due to the improved speed of the adiabatic calculation we could scan discrete values of both Δm_{21}^2 and E_{ν} , whereas the lookup table used previously was calculated at discrete values of $\Delta m_{21}^2/E_{\nu}$, which resulted in small but

observable discontinuities.

We also updated the electron density as a function of Earth radius, which affects the survival probability of neutrinos propagating through the Earth. Previous SNO analyses used the PREM [39] model, which averages over the continental and oceanic crust. When neutrinos enter the SNO detector from above they must have propagated through continental crust; therefore, we modified the Earth density profile to use PEM-C [40], which assumes continental crust for the outer most layer of the Earth. Because this significantly affected neutrinos only during a short period of each day, this had a negligible effect on the calculated neutrino survival probability.

VI.2. Analysis of solar neutrino and KamLAND data

To compare the ν_e survival probability parameters calculated in Section V with a neutrino oscillation prediction it was necessary to account for the sensitivity of the SNO detector. Table XXII in Appendix C gives $S(E_\nu)$, the predicted spectrum of E_ν detectable by the SNO detector after including all effects such as the energy dependence of the cross-sections, reaction thresholds, and analysis cuts, but not including neutrino oscillations. We multiplied $S(E_\nu)$ by the predicted neutrino oscillation hypothesis distortions, and fitted the resulting spectrum to $S(E_\nu)$ distorted by Equations 6 and 7. We then calculated the χ^2 between the results from this fit and our fit to the SNO data presented in Section V.2. This calculation used the uncertainties and correlation matrix from the fit to SNO data, but did not include the uncertainties from the fit to the distorted $S(E_\nu)$ as this does not represent a measurement uncertainty.

The χ^2 was calculated as a function of the neutrino oscillation parameters. The best fit was determined from the parameters resulting in the minimum χ^2 , and the uncertainties were calculated from the change in χ^2 from this minimum. Tests with simulated data revealed that this method produced neutrino oscillation parameters that were unbiased and produced uncertainties consistent with frequentist statistics.

The following additional solar neutrino results were used in calculating the results from solar neutrino experiments: the solar neutrino rates measured in Ga [41], and Cl [42] experiments, the rate of ${}^7\text{Be}$ solar neutrinos measured in Borexino [43], and the rates and recoil electron energy spectra of ${}^8\text{B}$ neutrino ES reactions measured in Borexino [44], SuperKamiokande-I [45], SuperKamiokande-II [46], and SuperKamiokande-III [47]. The last two SuperKamiokande results were split into day and night, and the first SuperKamiokande result was split into multiple periods of the day. The difference in the day and night rate of ${}^7\text{Be}$ solar neutrinos recently measured in Borexino [48], and the recent measurement of the ${}^8\text{B}$ neutrino spectrum in KamLAND [49], were not included, but these results would not significantly change

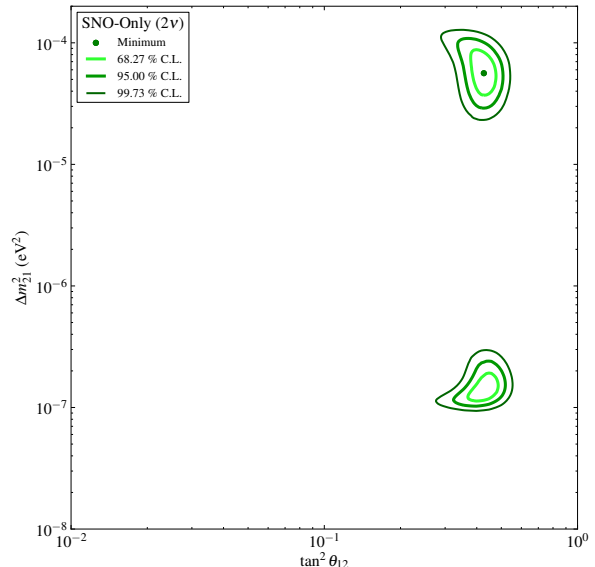


FIG. 14. Two-flavor neutrino oscillation analysis contour using only SNO data.

the results reported here. For a given set of neutrino oscillation parameters and Φ_B , the predictions for the set of experiments were calculated and compared to their results. This comparison was added to the χ^2 described above, and the resulting χ^2 was then minimized with respect to Φ_B . The same procedure as above was used to determine the best fit values and uncertainties.

The KamLAND experiment observed neutrino oscillations in $\bar{\nu}_e$ s from nuclear reactors. By assuming CPT invariance we can directly compare these results with the neutrino oscillations observed with solar neutrinos. Because this was a completely independent result, the lookup table of χ^2 as a function of θ_{12} , θ_{13} , and Δm^2_{21} published by the KamLAND collaboration [50] was added directly to the χ^2 values calculated from the solar neutrino analysis, and the same procedure was used to determine the best fit values and uncertainties.

VI.3. Two-flavor neutrino oscillation analysis

Figure 14 shows the allowed regions of the $(\tan^2 \theta_{12}, \Delta m^2_{21})$ parameter space obtained with the results in Tables VII and VIII. SNO data alone cannot distinguish between the upper (LMA) region, and the lower (LOW) region, although it slightly favors the LMA region.

Figure 15 shows the allowed regions of the $(\tan^2 \theta_{12}, \Delta m^2_{21})$ parameter space obtained when the SNO results were combined with the other solar neutrino experimental results, and when this combined solar neutrino result was combined with the results from the

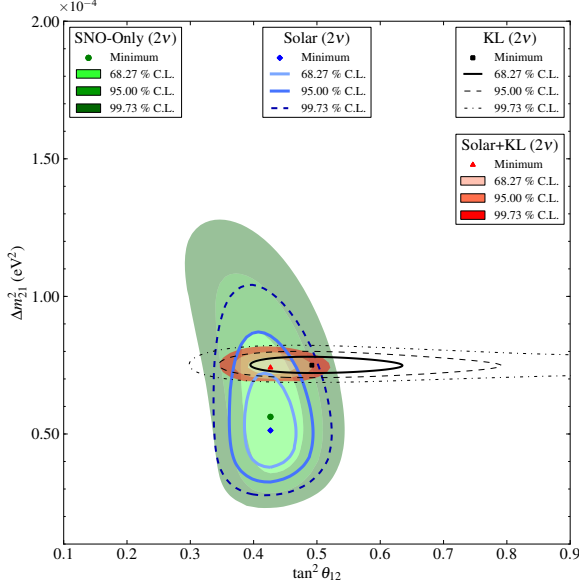


FIG. 15. Two-flavor neutrino oscillation analysis contour using both solar neutrino and KamLAND (KL) results.

KamLAND (KL) experiment. The combination of the SNO results with the other solar neutrino experimental results eliminates the LOW region, and eliminates the higher values of Δm_{21}^2 in the LMA region.

Table IX summarizes the results from these two-flavor neutrino analyses.

TABLE IX. Best-fit neutrino oscillation parameters from a two-flavor neutrino oscillation analysis. Uncertainties listed are $\pm 1\sigma$ after the χ^2 was minimized with respect to all other parameters.

Oscillation analysis	$\tan^2 \theta_{12}$	Δm_{21}^2 [eV ²]	χ^2/NDF
SNO only (LMA)	$0.427^{+0.033}_{-0.029}$	$5.62^{+1.32}_{-1.36} \times 10^{-5}$	1.39/3
SNO only (LOW)	$0.427^{+0.043}_{-0.035}$	$1.35^{+0.35}_{-0.14} \times 10^{-7}$	1.41/3
Solar	$0.427^{+0.028}_{-0.028}$	$5.13^{+1.29}_{-0.96} \times 10^{-5}$	108.07/129
Solar+KamLAND	$0.427^{+0.027}_{-0.024}$	$7.46^{+0.20}_{-0.19} \times 10^{-5}$	

VI.4. Three-flavor neutrino oscillation analysis

Figure 16 shows the allowed regions of the $(\tan^2 \theta_{12}, \Delta m_{21}^2)$ and $(\tan^2 \theta_{12}, \sin^2 \theta_{13})$ parameter spaces obtained from the results of all solar neutrino experiments. It also shows the result of these experiments combined with the results of the KamLAND experiment. Compared to the result in Figure 15, this clearly shows that allowing non-zero values of θ_{13} brings the solar neutrino experimental results into better agreement with the results from the KamLAND experiment.

Figure 17 shows the projection of these results onto the individual oscillation parameters. This result shows

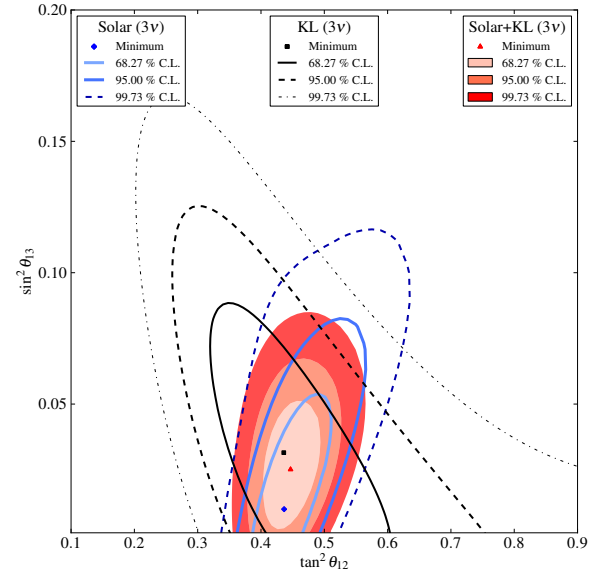
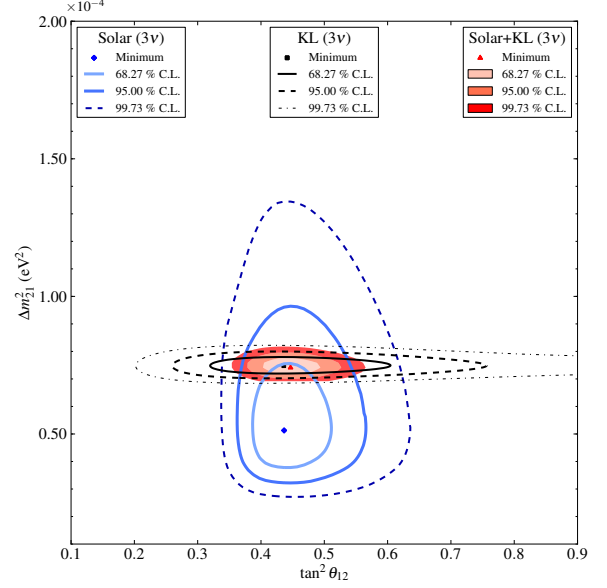


FIG. 16. Three-flavor neutrino oscillation analysis contour using both solar neutrino and KamLAND (KL) results.

that due to the different dependence between $\tan^2 \theta_{12}$ and $\sin^2 \theta_{13}$ for the solar neutrino experimental results and the KamLAND experimental results, the combined constraint on $\sin^2 \theta_{13}$ was significantly better than the individual constraints.

Table X summarizes the results from these three-flavor neutrino oscillation analyses. Tests with the inverted hierarchy, i.e. negative values of Δm_{31}^2 , gave essentially identical results [36].

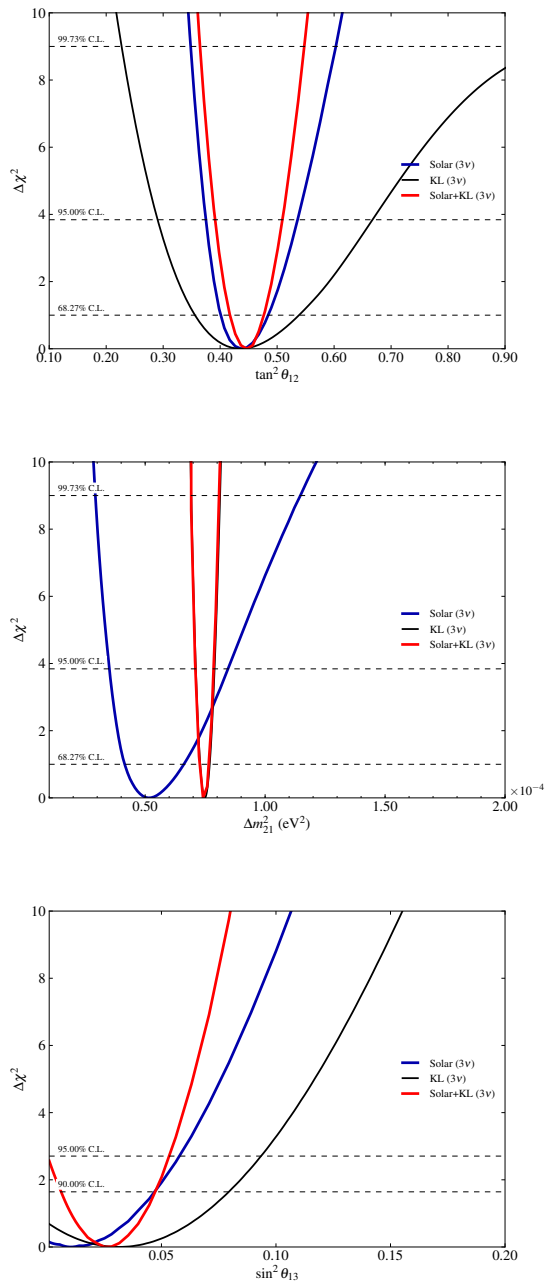


FIG. 17. Projections of the three-flavor neutrino oscillation parameters determined from Figure 16. The horizontal lines representing the $\Delta\chi^2$ for a particular confidence level, are for two-sided intervals in plot (a) and (b), and one-sided intervals in plot (c).

Figure 18 shows the measured solar ν_e survival probability as a function of E_ν . At higher E_ν the results of this analysis provide the best constraints on the survival probability. All solar results are consistent with the LMA neutrino oscillation hypothesis.

Recent results from the T2K [51] and MINOS [52] long-baseline (LBL) experiments indicate a non-zero θ_{13} with

TABLE X. Best-fit neutrino oscillation parameters from a three-flavor neutrino oscillation analysis. Uncertainties listed are $\pm 1\sigma$ after the χ^2 was minimized with respect to all other parameters. The global analysis includes Solar+KL+ATM+LBL+CHOOZ.

Analysis	$\tan^2 \theta_{12}$	Δm_{21}^2 [eV ²]	$\sin^2 \theta_{13}$ ($\times 10^{-2}$)
Solar	$0.436^{+0.048}_{-0.036}$	$5.13^{+1.49}_{-0.98} \times 10^{-5}$	< 5.8 (95% C.L.)
Solar+KL	$0.446^{+0.030}_{-0.029}$	$7.41^{+0.21}_{-0.19} \times 10^{-5}$	$2.5^{+1.8}_{-1.5}$ < 5.3 (95% C.L.)
Global			$2.02^{+0.88}_{-0.55}$

a significance of approximately 2.7σ . A combined analysis of all LBL and atmospheric (ATM) results, and the results from the CHOOZ [53] experiment was performed by Fogli *et al.* [54]. Because the LBL+ATM+CHOOZ analysis was insensitive to θ_{12} , and because the solar neutrino+KamLAND analysis was insensitive to Δm_{31}^2 we can simply add their projections of $\Delta\chi^2$ onto θ_{13} . Table X and Figure 19 show the results of that combination. This shows that the LBL+ATM+CHOOZ experiments currently have better sensitivity to θ_{13} than the combined solar and KamLAND experiments, but the combination of all experiments gives a slightly improved determination of θ_{13} , hinting at a non-zero value.

VII. DISCUSSION AND CONCLUSIONS

By developing a particle identification cut to analyze data from Phase III of the SNO experiment we measured 1115 ± 79 neutrons. Eliminating most of the background from alpha events and allowing a very general PDF to describe the E_{NCD} spectrum for any remaining background events made this analysis less sensitive to background uncertainties than our previous analysis of these data.

Combining data from all phases of the SNO experiment we measured a total flux of active flavor neutrinos from ^8B decays in the Sun of $(5.25 \pm 0.16(\text{stat.})^{+0.11}(\text{syst.})) \times 10^6 \text{ cm}^{-2}\text{s}^{-1}$. We improved the handling of a number of systematic uncertainties in this analysis compared with our previous analyses of these data. This result was consistent with but more precise than both the BPS09(GS), $(5.88 \pm 0.65) \times 10^6 \text{ cm}^{-2}\text{s}^{-1}$, and BPS09(AGSS09), $(4.85 \pm 0.58) \times 10^6 \text{ cm}^{-2}\text{s}^{-1}$, solar model predictions [6].

The precision of the ν_e survival probability parameters was improved by approximately 20% compared to our previously reported results due to the additional constraint provided by the data from Phase III. During the day the ν_e survival probability at 10 MeV was $c_0 = 0.317 \pm 0.016(\text{stat.}) \pm 0.009(\text{syst.})$, which was inconsistent with the null hypothesis that there were no neutrino oscillations at very high significance. The null hypotheses that there were no spectral distortions of the ν_e survival probability (i.e. $c_1 = 0$, $c_2 = 0$, $a_0 = 0$, $a_1 = 0$), and that there were no day/night distortions of the ν_e survival probability (i.e. $a_0 = 0$, $a_1 = 0$) could not be rejected at the 95% C.L.

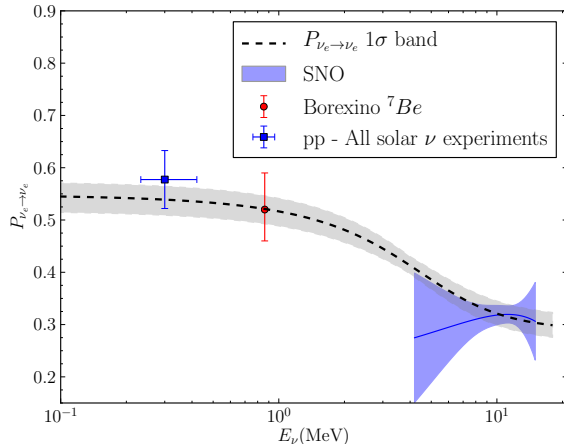


FIG. 18. Various solar ν_e survival probability measurements compared to the LMA prediction for ^8B neutrino. Using the results from Section VI of this paper, the dashed line is the best fit LMA solution for ^8B neutrinos and the gray shaded band is the 1σ uncertainty. The corresponding bands for ν_e s from the pp and ^7Be reactions (not shown) are almost identical in the region of those measurements. The blue shaded band is the result of the measurement the ^8B neutrino ν_e survival probability reported here. The red point is the result of the Borexino measurement [43] of the survival probability for ν_e s produced by $^7\text{Be} + e^- \rightarrow ^7\text{Li} + \nu_e$ reactions in the Sun. The blue point is the result of various measurements [41] of the survival probability for ν_e s produced by $p + p \rightarrow ^2\text{H} + e^+ + \nu_e$ reactions in the Sun; note that these measurements did not exclusively measure this reaction, so the contribution from other reactions were removed assuming the best fit LMA solution, and so actually depends on all solar neutrino results. The uncertainty in absolute flux of the subtracted reactions was included in the calculation of the total uncertainty of this point, but the uncertainty due to the neutrino oscillation probability of these reactions was not. The uncertainty due to the normalization of the two points by the expected flux was included. For clarity, this plot illustrates the LMA solution relative to only a subset of the solar neutrino experimental results.

A two-flavor neutrino oscillation analysis yielded $\Delta m_{21}^2 = (5.6_{-1.4}^{+1.9}) \times 10^{-5} \text{ eV}^2$ and $\tan^2 \theta_{12} = 0.427_{-0.029}^{+0.033}$. A three-flavor neutrino oscillation analysis combining this result with results of all other solar neutrino exper-

iments and the KamLAND experiment yielded $\Delta m_{21}^2 = (7.41_{-0.19}^{+0.21}) \times 10^{-5} \text{ eV}^2$, $\tan^2 \theta_{12} = 0.446_{-0.029}^{+0.030}$, and $\sin^2 \theta_{13} = (2.5_{-1.5}^{+1.8}) \times 10^{-2}$. This implied an upper bound of $\sin^2 \theta_{13} < 0.053$ at the 95% C.L.

VIII. ACKNOWLEDGMENTS

This research was supported by: Canada: Natural Sciences and Engineering Research Council, Industry Canada, National Research Council, Northern Ontario Heritage Fund, Atomic Energy of Canada, Ltd., Ontario

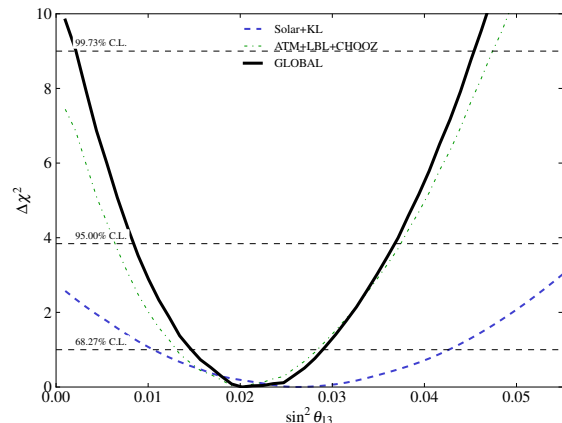


FIG. 19. Projection over $\sin^2 \theta_{13}$ combining the projections obtained by analyzing data from all neutrino sources. The data from atmospheric, short-baseline experiments and long-baseline experiments (ATM+LBL+CHOOZ) was determined from Figure 2-left of Reference [54] which already includes the latest T2K [51] and MINOS [52] results.

Power Generation, High Performance Computing Virtual Laboratory, Canada Foundation for Innovation, Canada Research Chairs; US: Department of Energy, National Energy Research Scientific Computing Center, Alfred P. Sloan Foundation; UK: Science and Technology Facilities Council; Portugal: Fundação para a Ciência e a Tecnologia. We thank the SNO technical staff for their strong contributions. We thank Vale (formerly Inco, Ltd.) for hosting this project.

^a Present address: Center for Astrophysics and Space Astronomy, University of Colorado, Boulder, CO

^b Present address: Institut für Kern- und Teilchenphysik, Technische Universität Dresden, Dresden, Germany

^c Present address: Department of Physics, University of California, Davis, CA

^d Present address: Institut für Experimentelle Kernphysik, Karlsruher Institut für Technologie, Karlsruhe, Germany

^e Present address: CERN, Geneva, Switzerland

^f Present address: Department of Physics, Hiroshima University, Hiroshima, Japan

^g Present address: Sanford Laboratory at Homestake, Lead, SD

^h Present address: Department of Physics, University of North Carolina, Chapel Hill, NC

ⁱ Present address: Center of Cosmology and Particle Astrophysics, National Taiwan University, Taiwan

^j Present address: Institute for Space Sciences, Freie Universität Berlin, Leibniz-Institute of Freshwater Ecology

and Inland Fisheries, Germany

- ^k Present address: Department of Physics and Astronomy, University of Alabama, Tuscaloosa, AL
- ^l Present address: Department of Physics, University of Liverpool, Liverpool, UK
- ^m Present address: Center for Experimental Nuclear Physics and Astrophysics, and Department of Physics, University of Washington, Seattle, WA
- ⁿ Present address: Dept. of Physics, University of California, Santa Barbara, CA
- ^o Present address: Dept. of Physics, Royal Holloway University of London, Egham, Surrey, UK
- ^p Address after January 2012: Physics Department, University of California at Berkeley, and Lawrence Berkeley National Laboratory, Berkeley, CA
- ^q Present address: Department of Physics and Astronomy, University of Sussex, Brighton, UK
- ^r Present address: Dept. of Chemistry and Physics, Armstrong Atlantic State University, Savannah, GA
- ^s Present address: CEA-Saclay, DSM/IRFU/SPP, Gif-sur-Yvette, France
- ^t Present address: Dept. of Physics, Queen's University, Kingston, Ontario, Canada
- ^u Present address: Physics Department, McGill University, Montreal, QC, Canada
- ^v Present address: Pacific Northwest National Laboratory, Richland, WA
- ^w Additional Address: Imperial College, London, UK
- ^x Present address: Dept. of Physics, Queen Mary University, London, UK
- ^y Deceased
- ^z Present address: Department of Physics, Princeton University, Princeton, NJ
- [1] H. H. Chen, Phys. Rev. Lett. **55**, 1534 (1985).
- [2] L. Wolfenstein, Phys. Rev. D **17**, 2369 (1978).
- [3] S. Mikheyev and A. Smirnov, Sov. J. Nucl. Phys. **42**, 913 (1985).
- [4] Z. Maki, M. Nakagawa, and S. Sakata, Prog. Theor. Phys. **28**, 870 (1962).
- [5] B. Pontecorvo, Sov. Phys.-JETP **7**, 172 (1958).
- [6] A. M. Serenelli, S. Basu, J. W. Ferguson, and M. Asplund, Astrophys. J. Lett. **705**, L123 (2009).
- [7] B. Aharmim *et al.* (SNO Collaboration), Phys. Rev. D **81**, 055504 (2010).
- [8] B. Aharmim *et al.* (SNO Collaboration), Phys. Rev. Lett. **101**, 111301 (2008).
- [9] J. Boger *et al.* (SNO Collaboration), Nucl. Inst. & Meth. **A449**, 172 (2000).
- [10] G. Doucas, S. Gil, N. A. Jelley, L. McGarry, M. E. Moorhead, N. W. Tanner, and C. E. Waltham, Nucl. Inst. & Meth. **A370**, 579 (1996).
- [11] B. Aharmim *et al.*, Nucl. Inst. & Meth. **A604**, 531 (2009).
- [12] J. F. Amsbaugh *et al.*, Nucl. Inst. & Meth. **A579**, 1054 (2007).
- [13] B. Aharmim *et al.* (SNO Collaboration), Phys. Rev. C **72**, 055502 (2005).
- [14] B. Aharmim *et al.*, (2011), arXiv:1107.2901 [nucl-ex].
- [15] Q. R. Ahmad *et al.* (SNO Collaboration), Phys. Rev. Lett. **89**, 011302 (2002).
- [16] In our previous analysis of data from Phases I and II [7] we described this method as imposing a unitarity constraint, which was not technically correct.
- [17] P.-L. Drouin, *Three-Phase Extraction of the Electron Neutrino Survival Probability at the Sudbury Neutrino Observatory*, Ph.D. thesis, Carleton University (2011), to be published.
- [18] T. C. Andersen *et al.*, Nucl. Inst. & Meth. **A501**, 386 (2003).
- [19] T. C. Andersen *et al.*, Nucl. Inst. & Meth. **A501**, 399 (2003).
- [20] H. M. O'Keefe *et al.*, Nucl. Inst. & Meth. (2011), in press, arXiv:1103.5788 [nucl-ex].
- [21] J. N. Bahcall, A. M. Serenelli, and S. Basu, Astrophys. J. Lett. **621**, L85 (2005).
- [22] M. R. Dragowsky *et al.*, Nucl. Inst. & Meth. **A481**, 284 (2002).
- [23] A. W. P. Poon, R. J. Komar, C. E. Waltham, M. C. Browne, R. G. H. Robertson, N. P. Kherani, and H. B. Mak, Nucl. Inst. & Meth. **A452**, 115 (2000).
- [24] N. J. Tagg, A. S. Hamer, B. Sur, E. D. Earle, R. L. Helmer, G. Jonkmans, B. A. Moffat, and J. J. Simpson, Nucl. Inst. & Meth. **A489**, 178 (2002).
- [25] K. Boudjemline *et al.*, Nucl. Inst. & Meth. **A620**, 171 (2010).
- [26] W. T. Winter, S. J. Freedman, K. E. Rehm, and J. P. Schiffer, Phys. Rev. C **73**, 025503 (2006).
- [27] F. James and M. Roos, Comp. Phys. Comm. **10**, 343 (1975).
- [28] S. Habib, *A Combined Three-Phase Signal Extraction of the Sudbury Neutrino Observatory Data Using Markov Chain Monte Carlo Technique*, Ph.D. thesis, University of Alberta (2011).
- [29] R. A. Ott, *Looking for Matter Enhanced Neutrino Oscillations Via Day v. Night Asymmetries in the NCD Phase of the Sudbury Neutrino Observatory*, Ph.D. thesis, Massachusetts Institute of Technology (2011).
- [30] B. Beltran *et al.*, New J. Phys. **13**, 073006 (2011).
- [31] N. S. Oblath, *A Measurement of Neutral-Current Neutrino Interactions at the Sudbury Neutrino Observatory with an Array of ^3He Proportional Counters*, Ph.D. thesis, University of Washington (2009).
- [32] R. Martin, *An Analysis of the ^3He Proportional Counter Data from the Sudbury Neutrino Observatory Using Pulse Shape Discrimination*, Ph.D. thesis, Queen's University (2009).
- [33] A. J. Wright, *Robust Signal Extraction Methods and Monte Carlo Sensitivity Studies for the Sudbury Neutrino Observatory and SNO+ Experiments*, Ph.D. thesis, Queen's University (2009).
- [34] Note that for these tests the PDF of E_{NCD} for neutron events was created from the ^{24}Na -2005 data, unlike the fit to real data, which used the ^{24}Na -2006 data.
- [35] <http://www.sno.phy.queensu.ca/papers/final8B/>.
- [36] N. Barros, *Precision measurement of neutrino oscillation parameters: combined three-phase results of the Sudbury Neutrino Observatory*, Ph.D. thesis, University of Lisbon (2011).
- [37] T. Schwetz, M. Tórtola, and J. W. F. Valle, New J. Phys. **13**, 063004 (2011).
- [38] <http://www.sns.ias.edu/%7Ejnb/SNdata/sndata.html>.
- [39] A. M. Dziewonski and D. L. Anderson, Phys. Earth Planet. In. **25**, 297 (1981).
- [40] A. M. Dziewonski, A. L. Hales, and E. R. Lapwood, Phys. Earth Planet. In. **10**, 12 (1975).
- [41] J. N. Abdurashitov *et al.* (SAGE Collaboration), Phys. Rev. C **80**, 015807 (2009), contains combined analysis

with the following references; M. Altmann *et al.* (GNO Collaboration), Physics Letters B **616**, 174 (2005); F. Kaether, *Datenanalyse der Sonnenneutrinoexperimente Gallex*, Ph.D. thesis, Heidelberg (2007).

- [42] B. T. Cleveland *et al.*, Astrophys. J. **496**, 505 (1998).
 [43] G. Bellini *et al.* (Borexino Collaboration), (2011), arXiv:1104.1816v1 [hep-ex].
 [44] G. Bellini *et al.* (Borexino Collaboration), Phys. Rev. D **82**, 033006 (2010).
 [45] J. Hosaka *et al.* (Super-Kamiokande Collaboration), Phys. Rev. D **73**, 112001 (2006).
 [46] J. P. Cravens *et al.* (Super-Kamiokande Collaboration), Phys. Rev. D **78**, 032002 (2008).
 [47] K. Abe *et al.* (Super-Kamiokande Collaboration), Phys. Rev. D **83**, 052010 (2011).
 [48] G. Bellini *et al.* (Borexino Collaboration), (2011), arXiv:1104.2150 [hep-ex].
 [49] S. Abe *et al.* (KamLAND Collaboration), (2011), arXiv:1106.0861 [hep-ex].
 [50] A. Gando *et al.* (KamLAND Collaboration), Phys. Rev. D **83**, 052002 (2011).
 [51] K. Abe *et al.* (T2K Collaboration), (2011), arXiv:1106.2822v1 [hep-ex].
 [52] P. Adamson *et al.* (MINOS Collaboration), (2011), arXiv:1108.0015 [hep-ex].
 [53] M. Apollonio *et al.*, Eur. Phys. J. C **27**, 331 (2003).
 [54] G. L. Fogli, E. Lisi, A. Marrone, A. Palazzo, and A. M. Rotunno, (2011), arXiv:1106.6028v1 [hep-ph].

Appendix A: Sterile neutrinos

If we assume a sterile neutrino, where the probability of an electron neutrino oscillating into a sterile neutrino, $P_{es}(E_\nu)$, was the same during the day and night, then the scaling factors given in Table I of Section III.1 are replaced with those in Table XI.

TABLE XI. ^8B neutrino interactions scaling factors including a probability of an electron neutrino oscillating into a sterile neutrino, which was the same during the day and night. $P_{ee}^n(E_\nu) = P_{ee}^d(E_\nu) \frac{2+A_{ee}(E_\nu)}{2-A_{ee}(E_\nu)}$, and $f(E_\nu)$ was the predicted spectrum of E_ν detectable by the SNO detector after including the energy dependence of the cross-section.

Interaction	Day/Night	Scaling factor
CC, ES _e	Day	$\Phi_B P_{ee}^d(E_\nu)$
ES _{$\mu\tau$}	Day	$\Phi_B [1 - P_{ee}^d(E_\nu) - P_{es}(E_\nu)]$
CC, ES _e	Night	$\Phi_B P_{ee}^n(E_\nu)$
ES _{$\mu\tau$}	Night	$\Phi_B [1 - P_{ee}^n(E_\nu) - P_{es}(E_\nu)]$
NC	Day+Night	$\Phi_B \frac{\int (1 - P_{es}(E_\nu)) f(E_\nu) dE_\nu}{\int f(E_\nu) dE_\nu}$

If $P_{es}(E_\nu)$ was a constant as a function of E_ν , and defining $\Phi_B' = \Phi_B(1 - P_{es}(E_\nu))$, and $P_{ee}^d(E_\nu)' = \frac{P_{ee}^d(E_\nu)}{1 - P_{es}(E_\nu)}$ we obtain the scaling factors given in Table XII.

Notice that scaling factors in Table XII are equivalent to those in Table I, except our measurement of the ^8B neutrino flux would be the true flux scaled by

TABLE XII. ^8B neutrino interactions scaling factors. $P_{ee}^n(E_\nu)' = P_{ee}^d(E_\nu)' \frac{2+A_{ee}(E_\nu)}{2-A_{ee}(E_\nu)}$.

Interaction	Day/Night	Scaling factor
CC, ES _e	Day	$\Phi_B' P_{ee}^d(E_\nu)'$
ES _{$\mu\tau$}	Day	$\Phi_B' [1 - P_{ee}^d(E_\nu)']$
CC, ES _e	Night	$\Phi_B' P_{ee}^n(E_\nu)'$
ES _{$\mu\tau$}	Night	$\Phi_B' [1 - P_{ee}^n(E_\nu)']$
NC	Day+Night	Φ_B'

$(1 - P_{es}(E_\nu))$ and our measurement of $P_{ee}^d(E_\nu)$ would be scaled by $1/(1 - P_{es}(E_\nu))$.

We note that the approximations made in this analysis were also valid for effects involving sterile neutrinos with spectral distortion that are significant only below about 4 MeV and with small day-night effects for the NC detection process. In this case the principal additional effect would be a further renormalization of the NC interaction rate.

Appendix B: Constraints on the likelihood fit

Systematic uncertainties were propagated on the PDFs as described in this section.

1. T_{eff} PDFs

Table XIII lists the systematic uncertainties on the PDFs of T_{eff} . For Phases I and II the modified T_{eff} , T_{eff}' , during the day was obtained from

$$T_{\text{eff}}' = (1 + a_0^E c + a_0^E - A_{dn}^E/2 - A_{dir}^E/2) T_{\text{eff}}. \quad (\text{B1})$$

The signs of the A_{dn}^E and A_{dir}^E terms were reversed for night. The uncertainty due to T_{eff} resolution was obtained by convolving T_{eff}' with Gaussians centered at zero with widths of σ^E , and σ_{dn}^E and σ_{dir}^E scaled by a parameterized detector resolution. This resolution was applied first to just day events and then to just night events. Differences in the neutrino parameters between the shifted fits and the central fit were taken as the resulting uncertainties.

During Phase III the modified T_{eff} , T_{eff}'' , was obtained from

$$T_{\text{eff}}'' = T_{\text{eff}}' + b_0^E (1 - B_{dir}^E/2) (T_{\text{eff}}' - T_g), \quad (\text{B2})$$

where T_g was the true MC energy. For the NC and external neutrons PDFs T_g was constant and equal to the mean fitter energy 5.65 MeV. T_{eff}' , was obtained from

$$T_{\text{eff}}' = (1 + a_0^E c + a_0^E) (1 - A_{dn}^E/2 - A_{dir}^E/2) T_{\text{eff}}, \quad (\text{B3})$$

where the signs of the A_{dn}^E and A_{dir}^E terms were reversed for night.

TABLE XIII. T_{eff} PDF systematic uncertainties.

Parameter	Description	Events	Phase	Nominal	Variation	Fit Value	Application
a_0^E	T_{eff} scale	all	I, II, III	0	± 0.0041	$0.0004^{+0.0033}_{-0.0024}$	scanned
a_0^E	T_{eff} scale	all	I	0	$+0.0039$	$-0.0007^{+0.0038}_{-0.0030}$	scanned
a_0^E	T_{eff} scale	all	II	0	-0.0047	$0.0001^{+0.0026}_{-0.0027}$	scanned
a_0^E	T_{eff} scale	all	III	0	± 0.0081	$0.0065^{+0.0042}_{-0.0084}$	scanned
c_0^E	T_{eff} scale non-linearity with T_{eff}	all	I, II, III	0	± 0.0069	N/A	shift-and-refit
A_{dn}^E	T_{eff} scale diurnal variation	all	I	0	± 0.0032	N/A	shift-and-refit
A_{dir}^E	T_{eff} scale directional variation	CC	I	0	$\pm 0.0009^a$	N/A	shift-and-refit
A_{dir}^E	T_{eff} scale directional variation	ES	I	0	$\pm 0.0092^a$	N/A	N/A
A_{dn}^E	T_{eff} scale diurnal variation	all	II	0	± 0.004	N/A	shift-and-refit
A_{dir}^E	T_{eff} scale directional variation	CC	II	0	$\pm 0.0009^b$	N/A	shift-and-refit
A_{dir}^E	T_{eff} scale directional variation	ES	II	0	$\pm 0.0079^b$	N/A	N/A
A_{dn}^E	T_{eff} scale diurnal variation	all	III	0	± 0.0038	$0.0005^{+0.0037}_{-0.0035}$	scanned
A_{dir}^E	T_{eff} scale directional variation	ES	III	0	± 0.0099	$-0.0038^{+0.0099}_{-0.0096}$	scanned
σ^E [MeV]	T_{eff} resolution	all	I	0.155	$+0.041$ -0.080	$0.214^{+0.023}_{-0.034}$	scanned
σ^E [MeV]	T_{eff} resolution	e^- , γ	II	0.168	$+0.041$ -0.080	$0.203^{+0.033}_{-0.041}$	scanned
σ^E [MeV]	T_{eff} resolution	n	II	0.154	± 0.018	$0.155^{+0.017}_{-0.019}$	scanned
b_0^E	T_{eff} resolution	n	III	0.0119	$\pm 0.0104^c$	$0.0109^{+0.0107}_{-0.0100}$	scanned
b_0^E	T_{eff} resolution	e^- , γ	III	0.016184	$\pm 0.0141^c$	N/A	N/A
σ_{dn}^E	T_{eff} resolution diurnal variation	all	I	0	± 0.003	N/A	shift-and-refit
σ_{dir}^E	T_{eff} resolution directional variation	CC	I	0	$\pm 0.0014^d$	N/A	shift-and-refit
σ_{dir}^E	T_{eff} resolution directional variation	ES	I	0	$\pm 0.0064^d$	N/A	N/A
σ_{dn}^E	T_{eff} resolution diurnal variation	all	II	0	± 0.005	N/A	shift-and-refit
σ_{dir}^E	T_{eff} resolution directional variation	CC	II	0	$\pm 0.0013^e$	N/A	shift-and-refit
σ_{dir}^E	T_{eff} resolution directional variation	ES	II	0	$\pm 0.013^e$	N/A	N/A
B_{dir}^E	T_{eff} resolution directional variation	ES	III	0	± 0.012	0.000 ± 0.012	scanned

^a Correlation of -1.

^b Correlation of -1.

^c Correlation of 1.

^d Correlation of -1.

^e Correlation of -1.

2. β_{14} PDFs

Table XIV lists the systematic uncertainties on the PDFs of β_{14} . During the day these uncertainties were applied using

$$\beta_{14}' = \beta_{14}(1 + a_0^{\beta_{14}} + c_0^{\beta_{14}}(T_{\text{eff}} - 5.589[\text{MeV}])) - A_{dn}^{\beta_{14}}/2 - A_{dir}^{\beta_{14}}/2. \quad (\text{B4})$$

The signs of the $A_{dn}^{\beta_{14}}$ and $A_{dir}^{\beta_{14}}$ terms were reversed for night. For electrons and γ -rays the systematic uncertainties associated with β_{14} resolution were applied as

$$\beta_{14}'' = \beta_{14}' + (\beta_{14}' - \bar{\beta}_{14})b_0^{\beta_{14}}, \quad (\text{B5})$$

where β_{14}'' was the value of β_{14} including all of the systematic uncertainties, and $\bar{\beta}_{14}$ a parameterized average value of β_{14} for the PDF. For neutrons in Phase II the systematic uncertainties associated with resolution were applied as a convolution with a Gaussian centered at zero with a width of $\sigma^{\beta_{14}}$. This correction can only be applied in the positive direction, and the negative fit uncertainties were inferred to be the same as the positive ones.

3. ρ PDFs

Table XV lists the systematic uncertainties on the PDFs of ρ . The radius was modified by

$$\rho'' = \frac{[(x''[\text{cm}])^2 + (y''[\text{cm}])^2 + (z''[\text{cm}])^2]^{3/2}}{600^3}, \quad (\text{B6})$$

where x'' , y'' , and z'' were the modified cartesian coordinates, as described below. Each event was weighted by a factor $1 + c^{\rho} \times (T_{\text{eff}} - 5.05[\text{MeV}])$.

During Phases I and II, x'' , y'' , and z'' , respectively, were obtained by convolving x' , y' , and z' with Gaussians centered at zero with widths of σ^x , σ^y , σ^z , σ_{dn}^{ρ} , or σ_{dir}^{ρ} . These resolutions were applied first to only day events and then to only night events. x' , y' , and z' were obtained from

$$x' = (1 + a_1^{\rho} - A_{dn}^{\rho}/2 - A_{dir}^{\rho}/2)(x + a_0^x) \quad (\text{B7})$$

$$y' = (1 + a_1^{\rho} - A_{dn}^{\rho}/2 - A_{dir}^{\rho}/2)(y + a_0^y) \quad (\text{B8})$$

$$z' = (1 + a_1^{\rho} + a_1^z - A_{dn}^{\rho}/2 - A_{dir}^{\rho}/2)(z + a_0^z). \quad (\text{B9})$$

The signs of the A_{dn}^{ρ} and A_{dir}^{ρ} terms were reversed for night.

TABLE XIV. β_{14} PDF systematic uncertainties.

Parameter	Description	Events	Phase	Nominal	Variation	Fit Value	Application
a_0^β	β_{14} scale	all	I	-0.0081	$\pm 0.0042^a$	N/A	scanned
a_0^β	β_{14} scale	e ⁻	II	0	$\pm 0.0024^a$	$0.00102^{+0.00112}_{-0.00205}$	N/A
a_0^β	β_{14} scale	n	II	-0.0144	$+0.0038$ -0.0022	$-0.0138^{+0.0036}_{-0.0025}$	scanned
c_0^β	β_{14} scale non-linearity with T_{eff}	all	I, II	0.00275597	± 0.00069	$0.00201^{+0.00058}_{-0.00044}$	scanned
A_{dn}^β	β_{14} offset diurnal variation	all	I	0	± 0.0043	N/A	shift-and-refit
A_{dir}^β	β_{14} offset directional variation	CC	I	0	$\pm 0.00038^b$	N/A	shift-and-refit
A_{dn}^β	β_{14} offset diurnal variation	ES	I	0	$\pm 0.0034^b$	N/A	N/A
A_{dn}^β	β_{14} offset diurnal variation	all	II	0	± 0.0043	N/A	shift-and-refit
A_{dir}^β	β_{14} offset directional variation	CC	II	0	$\pm 0.00038^c$	N/A	shift-and-refit
A_{dir}^β	β_{14} offset directional variation	ES	II	0	$\pm 0.0034^c$	N/A	N/A
b_0^β	β_{14} resolution	all	I	0	$\pm 0.0042^d$	N/A	shift-and-refit
b_0^β	β_{14} resolution	e ⁻	II	0	$\pm 0.0054^d$	N/A	N/A
σ^β	β_{14} resolution	n	II	0.0150	± 0.0045	N/A	shift-and-refit

^a Correlation of 1.

^b Correlation of -1.

^c Correlation of -1.

^d Correlation of 1.

During Phase III the uncertainties were applied as

$$x'' = x' + (b_0^{x,y} + b_1^{x,y}z + b_2^{x,y}z^2)(x' - x_g) \quad (\text{B10})$$

$$y'' = y' + (b_0^{x,y} + b_1^{x,y}z + b_2^{x,y}z^2)(y' - y_g) \quad (\text{B11})$$

$$z'' = z' + (b_0^z + b_1^z z)(z' - z_g), \quad (\text{B12})$$

where x_g, y_g, z_g were the true MC positions. x', y' , and z' were obtained from

$$x' = (1 + a_1^\rho)(1 - A_{dn}/2 - A_{dir}/2)(x + a_0^x) \quad (\text{B13})$$

$$y' = (1 + a_1^\rho)(1 - A_{dn}/2 - A_{dir}/2)(y + a_0^y) \quad (\text{B14})$$

$$z' = (1 + a_1^\rho + a_1^z)(1 - A_{dn}/2 - A_{dir}/2)(z + a_0^z). \quad (\text{B15})$$

The signs of the A_{dn}^ρ and A_{dir}^ρ terms were reversed for night.

4. $\cos \theta_\odot$ PDFs

Table XVI lists the systematic uncertainties on the PDFs of $\cos \theta_\odot$. For Phases I and II the modified $\cos \theta_\odot$, $\cos \theta_\odot'$, was obtained from

$$\cos \theta_\odot' = 1 + (1 + a_0^\theta - A_{dir}^\theta/2)(\cos \theta_\odot - 1). \quad (\text{B16})$$

For Phase III the modified $\cos \theta_\odot$, $\cos \theta_\odot'$, was obtained from

$$\cos \theta_\odot' = 1 + (1 + a_0^\theta)(1 - A_{dir}^\theta/2)(\cos \theta_\odot - 1) \quad (\text{B17})$$

If the transformation moved $\cos \theta_\odot'$ outside the range $[-1, 1]$, $\cos \theta_\odot'$ was given a random value within this interval.

5. E_{NCD} PDFs

Table XVII lists the systematic uncertainties on the PDFs of E_{NCD} . The modified E_{NCD} , E_{NCD}' , was ob-

tained from

$$E_{\text{NCD}}' = (1 + a_1^{E_{\text{NCD}}})E_{\text{NCD}}. \quad (\text{B18})$$

For each event in the PDF one hundred random numbers drawn from a Gaussian centered at zero with a width of $b_0^{E_{\text{NCD}}} E_{\text{NCD}}$ were used to construct a new PDF.

6. Background constraints

Table XVIII gives the constraints on the backgrounds in Phases I and II. Table XIX gives the constraints on the backgrounds in Phase III.

7. PMT background PDF

Table XX shows the constraints on the analytical PDF given by Equation 10 in Section III.3 for PMT background events.

8. Neutron detection efficiencies

Table XXI shows the constraints on the neutron detection efficiencies. NC interactions observed with the PMT array in Phases I and II were weighted by

$$1 + \epsilon_n^{\text{PMT}} + \epsilon_{n,\text{corr.}}^{\text{PMT}}. \quad (\text{B19})$$

NC interactions observed with the PMT array in Phase III were weighted by

$$1 + \epsilon_n^{\text{PMT}}. \quad (\text{B20})$$

NC interactions observed with the NCD array in Phase III were weighted by

$$1 + \epsilon_n^{\text{NCD}}. \quad (\text{B21})$$

TABLE XV. ρ PDF systematic uncertainties.

Parameter	Description	Events	Phase	Nominal	Variation	Fit Value	Application
a_1^ρ	ρ scale	all	I	0	+0.0010 -0.0057	N/A	shift-and-refit
a_1^z	z scale	all	I	0	+0.0040 -0.0	N/A	shift-and-refit
a_1^ρ	ρ scale	all	II	0	+0.0004 -0.0034	N/A	shift-and-refit
a_1^z	z scale	all	II	0	+0.0003 -0.0025	N/A	shift-and-refit
a_1^ρ	ρ scale	all	III	0	+0.0029 -0.0077	0.0004 ^{+0.0027} _{-0.0051}	scanned
a_1^z	z scale	all	III	0	+0.0015 -0.0012	N/A	shift-and-refit
c^ρ	ρ scale non-linearity with T_{eff}	all	I	0	+0.0085 -0.0049	N/A	shift-and-refit
c^ρ	ρ scale non-linearity with T_{eff}	all	II	0	+0.0041 -0.0048	N/A	shift-and-refit
c^ρ	ρ scale non-linearity with T_{eff}	all	III	0	+0.0088 -0.0067	N/A	shift-and-refit
A_{dn}^ρ	ρ scale diurnal variation	all	I	0	± 0.002	N/A	shift-and-refit
A_{dn}^ρ	ρ scale directional variation	CC	I	0	$\pm 0.0004^a$	N/A	shift-and-refit
$A_{dn}^{\beta_{dir}}$	ρ scale directional variation	ES	I	0	$\pm 0.005^a$	N/A	N/A
A_{dn}^ρ	ρ scale diurnal variation	all	II	0	± 0.003	N/A	shift-and-refit
A_{dn}^ρ	ρ scale directional variation	CC	II	0	$\pm 0.0002^b$	N/A	shift-and-refit
$A_{dn}^{\beta_{dir}}$	ρ scale directional variation	ES	II	0	$\pm 0.0015^b$	N/A	N/A
A_{dn}^ρ	ρ scale diurnal variation	all	III	0	± 0.0015	N/A	shift-and-refit
$A_{dn}^{\beta_{dir}}$	ρ scale directional variation	ES	III	0	± 0.0018	N/A	shift-and-refit
a_0^x [cm]	x shift	all	I	0	+1.15 -0.13	N/A	shift-and-refit
a_0^y [cm]	y shift	all	I	0	+2.87 -0.17	N/A	shift-and-refit
a_0^z [cm]	z shift	all	I	5	+2.58 -0.15	N/A	shift-and-refit
a_0^x [cm]	x shift	all	II	0	+0.92 -0.07	N/A	shift-and-refit
a_0^y [cm]	y shift	all	II	0	+2.29 -0.09	N/A	shift-and-refit
a_0^z [cm]	z shift	all	II	5	+3.11 -0.16	N/A	shift-and-refit
a_0^x [cm]	x shift	all	III	0	± 4.0	N/A	shift-and-refit
a_0^y [cm]	y shift	all	III	0	± 4.0	N/A	shift-and-refit
a_0^z [cm]	z shift	all	III	5	± 4.0	N/A	shift-and-refit
σ^x [cm]	x resolution	all	I	0	± 3.3	N/A	shift-and-refit
σ^y [cm]	y resolution	all	I	0	± 2.2	N/A	shift-and-refit
σ^z [cm]	z resolution	all	I	0	± 1.5	N/A	shift-and-refit
σ^x [cm]	x resolution	all	II	0	± 3.1	N/A	shift-and-refit
σ^y [cm]	y resolution	all	II	0	± 3.4	N/A	shift-and-refit
σ^z [cm]	z resolution	all	II	0	± 5.3	N/A	shift-and-refit
$b_0^{x,y}$	x, y resolution constant term	all	III	0.065	$\pm 0.029^c$	N/A	shift-and-refit
$b_1^{x,y}$ [cm ⁻¹]	x, y resolution linear term	all	III	-5.5×10^{-5}	$\pm 6.1 \times 10^{-3c}$	N/A	shift-and-refit
$b_2^{x,y}$ [cm ⁻²]	x, y resolution quadratic term	all	III	3.9×10^{-7}	$\pm 2.0 \times 10^{-7c}$	N/A	shift-and-refit
b_0^z	z resolution constant term	all	III	0.0710	$\pm 0.028^d$	N/A	shift-and-refit
b_1^z [cm ⁻¹]	z resolution linear term	all	III	1.16×10^{-4}	$\pm 0.83 \times 10^{-4d}$	N/A	shift-and-refit
σ_{dn}^ρ [cm]	ρ resolution diurnal variation	all	I	0	± 6.82	N/A	shift-and-refit
σ_{dn}^ρ [cm]	ρ resolution diurnal variation	all	II	0	± 7.21	N/A	shift-and-refit
$\sigma_{dn}^{\beta_{dir}}$ [cm]	ρ resolution directional variation	CC	II	0	$\pm 1.02^e$	N/A	shift-and-refit
$\sigma_{dir}^{\beta_{dir}}$ [cm]	ρ resolution directional variation	ES	II	0	$\pm 3.36^e$	N/A	N/A

^a Correlation of -1.

^b Correlation of -1.

^c Correlation of $\begin{pmatrix} 1 & -0.13 & -0.74 \\ -0.13 & 1 & 0.31 \\ -0.74 & 0.31 & 1 \end{pmatrix}$.

^d Correlation of 0.15.

^e Correlation of -1.

Background neutrons from photo-disintegration observed with the PMT array in Phases I and II were weighted by

$$(1 + \epsilon_n^{\text{PMT}} + \epsilon_{n,\text{corr}}^{\text{PMT}})(1 + \epsilon_{\text{PD}}). \quad (\text{B22})$$

This uncertainty was already included in the rates of these backgrounds in Table XIX for Phase III.

Appendix C: Neutrino sensitivity

Table XXII gives $S(E_\nu)$, the predicted spectrum of E_ν detectable by the SNO detector after including all effects such as the energy dependence of the cross-sections, reaction thresholds, and analysis cuts, but not including neutrino oscillations.

TABLE XVI. $\cos\theta_{\odot}$ PDF systematic uncertainties.

Parameter	Description	Events	Phase	Nominal	Variation	Fit Value	Application
a_0^θ	$\cos\theta_{\odot}$ scale	ES	I	0	± 0.11	N/A	shift-and-refit
a_0^θ	$\cos\theta_{\odot}$ scale	ES	II	0	± 0.11	N/A	shift-and-refit
a_0^θ	$\cos\theta_{\odot}$ scale	ES	III	0	± 0.12	$0.063^{+0.104}_{-0.099}$	scanned
A_{dir}^θ	$\cos\theta_{\odot}$ scale directional variation	ES	I	0	± 0.022	N/A	shift-and-refit
A_{dir}^θ	$\cos\theta_{\odot}$ scale directional variation	ES	II	0	± 0.052	N/A	shift-and-refit
A_{dir}^θ	$\cos\theta_{\odot}$ scale directional variation	ES	III	0	± 0.069	$-0.015^{+0.073}_{-0.066}$	scanned

TABLE XVII. E_{NCD} PDF systematic uncertainties.

Parameter	Description	Events	Phase	Nominal	Variation
$a_1^{E_{\text{NCD}}}$	E_{NCD} scale	n	III	0	± 0.01
$b_0^{E_{\text{NCD}}}$	E_{NCD} resolution	n	III	0	$^{+0.01}_{-0.00}$

TABLE XVIII. Background constraints in Phases I and II. The constraints were all applied to the combined day + night value.

Background	Phase	Constraint	Fit Value		Application
			Day	Night	
Internal ^{214}Bi [mBq]	I	126^{+42}_{-25}	$64.9^{+7.2}_{-7.1}$	$96.1^{+6.9}_{-6.9}$	floated
Internal ^{208}Tl [mBq]	I	$3.1^{+1.4}_{-1.3}$	$1.11^{+0.37}_{-0.36}$	$1.09^{+0.35}_{-0.34}$	floated
External ^{214}Bi [Bq]	I	6.50 ± 1.11	$11.9^{+4.2}_{-4.2}$	$2.9^{+3.3}_{-3.4}$	floated
External ^{208}Tl [Bq]	I	$0.190^{+0.063}_{-0.054}$	$0.153^{+0.202}_{-0.199}$	$0.265^{+0.157}_{-0.157}$	floated
PMT [Arb.]	I	N/A	$0.938^{+0.072}_{-0.071}$	$1.018^{+0.059}_{-0.058}$	floated
AV surface neutrons [Arb.]	I	N/A	$3.026^{+1.499}_{-1.477}$	^a	floated
AV ^{214}Bi [Arb.]	I	N/A	$2.522^{+2.252}_{-2.164}$	^a	floated
AV ^{208}Tl [Arb.]	I	N/A	$6.196^{+1.318}_{-1.315}$	^a	floated
<i>hep</i> neutrino [events]	I	15^{b}	N/A	N/A	fixed
Other <i>n</i> [events]	I	$3.2 \pm 0.8^{\text{c}}$	N/A	N/A	shift-and-refit
Atmospheric ν [events]	I	21.3 ± 4.0	N/A	N/A	shift-and-refit
AV instrumental background [events]	I	$0.00^{+24.49}_{-0}^{\text{d}}$	N/A	N/A	shift-and-refit
Internal ^{214}Bi [Arb.]	II	N/A	$0.742^{+0.074}_{-0.074}$	$0.495^{+0.067}_{-0.067}$	floated
Internal ^{208}Tl [mBq]	II	$2.6^{+1.2}_{-1.5}$	$0.69^{+1.68}_{-1.68}$	$1.49^{+1.41}_{-1.41}$	floated
Internal ^{24}Na [mBq]	II	0.245 ± 0.060	$0.274^{+0.342}_{-0.342}$	$0.193^{+0.284}_{-0.285}$	floated
External ^{214}Bi [Bq]	II	4.36 ± 1.05	$4.56^{+3.35}_{-3.35}$	$5.15^{+2.86}_{-2.86}$	floated
External ^{208}Tl [Bq]	II	0.129 ± 0.040	$0.216^{+0.159}_{-0.160}$	$0.071^{+0.135}_{-0.133}$	floated
PMT [Arb.]	II	N/A	$1.093^{+0.053}_{-0.053}$	$1.244^{+0.049}_{-0.049}$	floated
AV surface neutrons [Arb.]	II	N/A	$-0.359^{+0.473}_{-0.468}$	^a	floated
AV ^{214}Bi [Arb.]	II	N/A	$0.821^{+1.486}_{-1.439}$	^a	floated
AV ^{208}Tl [Arb.]	II	N/A	$6.218^{+0.981}_{-0.979}$	^a	floated
<i>hep</i> neutrino [events]	II	33^{b}	N/A	N/A	fixed
Other <i>n</i> [events]	II	$12.0 \pm 3.1^{\text{c}}$	N/A	N/A	shift-and-refit
Atmospheric ν [events]	II	29.8 ± 5.7	N/A	N/A	shift-and-refit
AV instrumental background [events]	II	$0.00^{+36.19}_{-0}^{\text{d}}$	N/A	N/A	shift-and-refit

^a The fit was performed with day+night combined, so there is only one fit value for both.^b Fixed at CC=0.35 SSM, ES=0.47 SSM, NC=1.0 SSM [21].^c Correlation 1.^d One-sided, effect is symmetrized.

TABLE XIX. Background constraints in Phase III. The constraints were applied on the number of events observed in the NCD array. The number of events observed in the PMT array were obtained from the number of events in the NCD array multiplied by the PMT array ratio.

Background	NCD Array		PMT Array ratio	D/N asymmetry	
	Constraint	Fit Value		Constraint	Fit Value
External + AV	40.9 ± 20.6	38.1 ± 19.2	0.5037	-0.020 ± 0.011	-0.019 ± 0.011
Internal	31.0 ± 4.7	30.9 ± 4.8	0.2677	-0.034 ± 0.112	-0.034 ± 0.112
NCD bulk ^a	27.6 ± 11.0	27.2 ± 9.4	0.1667	0	N/A
K2 hotspot	32.8 ± 5.3	32.6 ± 5.2	0.2854	0	N/A
K5 hotspot	$45.5^{+7.5}_{-8.4}$	$45.4^{+7.5}_{-8.3}$	0.2650	0	N/A
NCD array cables ^a	8.0 ± 5.2		0.1407	0	N/A
Atmospheric ν and cosmogenic muons	13.6 ± 2.7	13.4 ± 2.7	1.8134	0	N/A

^a In the previous analysis of data from Phase III [8] these two backgrounds were combined.

TABLE XX. PMT background PDF parameters for the analytical PDF given by Equation 10 in Section III.3.

Parameter	Phase	Day/Night	Constraint	Fit Value	Application
ϵ	I	day	-6.73 ± 1.29	$-6.30^{+0.35}_{-0.55}$	scanned
ϵ	I	night	-5.64 ± 1.02	$-6.40^{+0.31}_{-0.46}$	scanned
ϵ	II	day	-6.26 ± 0.91	$-6.78^{+0.29}_{-0.37}$	scanned
ϵ	II	night	-6.98 ± 0.91	$-6.72^{+0.24}_{-0.33}$	scanned
η_1^a	I	day	0 ± 1	$-0.74^{+1.10}_{-0.54}$	scanned
η_1^b	I	night	0 ± 1	$-0.39^{+0.39}_{-0.12}$	scanned
η_1^c	II	day	0 ± 1	$0.74^{+0.42}_{-0.26}$	scanned
η_1^d	II	night	0 ± 1	$0.31^{+0.26}_{-0.13}$	scanned
η_2^a	I	day	0 ± 1	$0.09^{+0.62}_{-0.61}$	scanned
η_2^b	I	night	0 ± 1	$0.08^{+0.77}_{-0.78}$	scanned
η_2^c	II	day	0 ± 1	$-2.42^{+0.91}_{-0.39}$	scanned
η_2^d	II	night	0 ± 1	$-3.73^{+0.47}_{-0.49}$	scanned
ω_0	I	day	0.533 ± 0.014	$0.5351^{+0.0090}_{-0.0083}$	scanned
ω_0	I	night	0.533 ± 0.014	$0.5469^{+0.0071}_{-0.0072}$	scanned
ω_0	II	day	0.511 ± 0.007	$0.5096^{+0.0055}_{-0.0047}$	scanned
ω_0	II	night	0.511 ± 0.007	$0.5119^{+0.0049}_{-0.0055}$	scanned
ω_1	I	day	0.237 ± 0.051	N/A	shift-and-refit
ω_1	I	night	0.237 ± 0.051	N/A	shift-and-refit
ω_1	II	day	0.182 ± 0.095	N/A	shift-and-refit
ω_1	II	night	0.182 ± 0.095	N/A	shift-and-refit
β_s	I	day	0.182 ± 0.011	N/A	shift-and-refit
β_s	I	night	0.182 ± 0.011	N/A	shift-and-refit
β_s	II	day	0.195 ± 0.007	N/A	shift-and-refit
β_s	II	night	0.195 ± 0.007	N/A	shift-and-refit

^a $b = -1.00 + 1.29\eta_1$, $\nu = 6.63 + 0.93 * (0.60 * \eta_1 + \sqrt{1 - 0.60^2}\eta_2)$

^b $b = 3.27 + 12.04\eta_1$, $\nu = 6.78 + 1.52 * (0.96 * \eta_1 + \sqrt{1 - 0.96^2}\eta_2)$

^c $b = -0.33 + 2.08\eta_1$, $\nu = 5.32 + 1.01 * (0.91 * \eta_1 + \sqrt{1 - 0.91^2}\eta_2)$

^d $b = 0.49 + 3.02\eta_1$, $\nu = 5.66 + 1.07 * (0.94 * \eta_1 + \sqrt{1 - 0.94^2}\eta_2)$

TABLE XXI. Uncertainties in the neutron detection and photo-disintegration backgrounds.

Parameter	Description	Phase	Constraint	Fit Value	Application
ϵ_n^{PMT}	Neutron detection in the PMT array	I	0 ± 0.0187	N/A	shift-and-refit
ϵ_n^{PMT}	Neutron detection in the PMT array	II	0 ± 0.0124	N/A	shift-and-refit
$\epsilon_n^{\text{PMT,corr.}}$	Correlated neutron detection in the PMT array	I, II	0 ± 0.007	N/A	shift-and-refit
ϵ_n^{PMT}	Neutron detection in the PMT array	III	0 ± 0.028	-0.003 ± 0.028	float
ϵ_n^{NCD}	Neutron detection in the NCD array	III	0 ± 0.024	-0.001 ± 0.023	float
ϵ_{PD}	Photo-disintegration	I, II	0 ± 0.02	N/A	shift-and-refit

TABLE XXII. Predicted spectrum of E_ν detectable by the SNO detector after including all effects such as the energy dependence of the cross-sections, reaction thresholds, and analysis cuts, but not including neutrino oscillations, $S(E_\nu)$. The number of events are for all three phases combined and assumes the BS05(OP) solar neutrino model ($\Phi_B=5.69 \times 10^6 \text{ cm}^{-2}\text{s}^{-1}$) [21].

E_ν range [MeV]	CC		ES _e		ES _{$\mu\tau$}		E_ν range [MeV]	CC		ES _e		ES _{$\mu\tau$}	
	day	night	day	night	day	night		day	night	day	night	day	night
2.9-3.0	0.0	0.0	0.0	0.1	0.0	0.0	9.1-9.2	185.3	231.3	19.9	24.8	3.2	4.0
3.0-3.1	0.0	0.0	0.1	0.1	0.0	0.0	9.2-9.3	187.7	235.1	20.1	24.6	3.2	4.0
3.1-3.2	0.0	0.0	0.1	0.1	0.0	0.0	9.3-9.4	191.3	238.8	20.0	24.7	3.2	4.0
3.2-3.3	0.0	0.0	0.1	0.2	0.0	0.0	9.4-9.5	194.0	241.2	20.1	24.8	3.2	3.9
3.3-3.4	0.0	0.0	0.2	0.2	0.0	0.0	9.5-9.6	196.4	244.4	19.7	24.4	3.2	3.9
3.4-3.5	0.0	0.0	0.3	0.3	0.0	0.1	9.6-9.7	198.6	246.1	19.9	24.5	3.2	3.9
3.5-3.6	0.0	0.0	0.4	0.5	0.1	0.1	9.7-9.8	199.7	249.3	19.5	24.2	3.1	3.9
3.6-3.7	0.0	0.0	0.5	0.6	0.1	0.1	9.8-9.9	199.8	250.2	19.4	24.0	3.1	3.9
3.7-3.8	0.0	0.0	0.6	0.7	0.1	0.1	9.9-10.0	200.1	251.1	19.3	23.7	3.1	3.8
3.8-3.9	0.0	0.0	0.8	0.9	0.1	0.2	10.0-10.1	200.9	251.0	19.0	23.5	3.0	3.7
3.9-4.0	0.0	0.1	0.9	1.2	0.2	0.2	10.1-10.2	200.8	250.8	18.7	23.1	3.0	3.7
4.0-4.1	0.1	0.1	1.1	1.5	0.2	0.2	10.2-10.3	199.7	248.7	18.5	22.9	2.9	3.6
4.1-4.2	0.1	0.2	1.4	1.6	0.2	0.3	10.3-10.4	198.3	246.8	18.1	22.3	2.9	3.6
4.2-4.3	0.3	0.3	1.6	2.0	0.3	0.3	10.4-10.5	198.0	246.5	17.7	21.9	2.9	3.5
4.3-4.4	0.4	0.5	1.9	2.4	0.3	0.4	10.5-10.6	195.4	244.5	17.3	21.4	2.8	3.4
4.4-4.5	0.6	0.8	2.2	2.7	0.4	0.4	10.6-10.7	193.9	241.6	17.0	21.1	2.7	3.4
4.5-4.6	1.0	1.2	2.5	3.1	0.4	0.5	10.7-10.8	191.7	237.5	16.5	20.6	2.6	3.3
4.6-4.7	1.4	1.8	2.8	3.5	0.5	0.6	10.8-10.9	187.1	233.2	16.2	19.8	2.6	3.2
4.7-4.8	2.0	2.7	3.1	3.9	0.5	0.6	10.9-11.0	184.4	229.6	15.9	19.4	2.5	3.1
4.8-4.9	2.8	3.6	3.5	4.5	0.6	0.7	11.0-11.1	180.5	226.4	15.3	18.8	2.4	3.0
4.9-5.0	3.8	4.8	3.9	4.8	0.6	0.8	11.1-11.2	176.6	220.0	14.7	18.3	2.3	2.9
5.0-5.1	4.9	6.3	4.4	5.3	0.7	0.9	11.2-11.3	172.2	214.3	14.2	17.5	2.3	2.8
5.1-5.2	6.4	8.0	4.7	5.9	0.8	1.0	11.3-11.4	167.8	208.2	13.6	16.8	2.2	2.7
5.2-5.3	8.0	10.2	5.2	6.4	0.8	1.0	11.4-11.5	162.4	202.7	13.1	16.3	2.1	2.6
5.3-5.4	10.0	12.7	5.7	6.9	0.9	1.1	11.5-11.6	157.5	195.9	12.6	15.6	2.0	2.5
5.4-5.5	12.3	15.5	6.1	7.6	1.0	1.2	11.6-11.7	152.2	188.9	12.0	14.9	1.9	2.4
5.5-5.6	14.5	18.7	6.6	8.1	1.0	1.3	11.7-11.8	146.5	181.8	11.4	14.2	1.8	2.3
5.6-5.7	17.4	22.1	7.1	8.8	1.1	1.4	11.8-11.9	139.9	173.9	11.0	13.4	1.7	2.1
5.7-5.8	20.3	26.1	7.5	9.2	1.2	1.5	11.9-12.0	133.7	166.4	10.3	12.7	1.7	2.0
5.8-5.9	23.4	29.9	8.0	9.9	1.3	1.6	12.0-12.1	127.0	158.4	9.7	12.1	1.5	1.9
5.9-6.0	26.9	34.3	8.4	10.4	1.3	1.7	12.1-12.2	121.2	149.8	8.9	11.5	1.5	1.8
6.0-6.1	30.8	39.0	9.0	11.2	1.4	1.8	12.2-12.3	114.0	141.5	8.5	10.6	1.4	1.7
6.1-6.2	34.5	44.0	9.6	11.8	1.5	1.9	12.3-12.4	107.1	133.2	8.0	9.8	1.3	1.6
6.2-6.3	38.5	49.2	10.0	12.4	1.6	2.0	12.4-12.5	100.3	124.8	7.4	9.2	1.2	1.5
6.3-6.4	42.5	54.0	10.6	13.1	1.7	2.1	12.5-12.6	93.3	116.6	6.8	8.6	1.1	1.4
6.4-6.5	47.3	59.4	11.0	13.6	1.8	2.2	12.6-12.7	87.0	108.3	6.3	7.8	1.0	1.3
6.5-6.6	51.5	65.7	11.5	14.3	1.8	2.3	12.7-12.8	80.7	99.6	5.9	7.1	0.9	1.1
6.6-6.7	56.3	71.8	12.1	15.0	1.9	2.4	12.8-12.9	73.3	91.6	5.2	6.5	0.8	1.0
6.7-6.8	61.3	77.2	12.5	15.5	2.0	2.5	12.9-13.0	66.9	83.0	4.7	5.8	0.8	0.9
6.8-6.9	66.2	83.1	13.1	16.3	2.1	2.6	13.0-13.1	60.3	75.0	4.3	5.3	0.7	0.8
6.9-7.0	70.5	89.9	13.6	16.6	2.2	2.7	13.1-13.2	54.3	67.3	3.8	4.7	0.6	0.8
7.0-7.1	75.7	96.7	14.1	17.5	2.3	2.8	13.2-13.3	48.2	59.9	3.3	4.2	0.5	0.7
7.1-7.2	81.1	103.4	14.5	18.2	2.3	2.9	13.3-13.4	42.4	52.5	2.9	3.7	0.5	0.6
7.2-7.3	86.8	109.3	15.1	18.5	2.4	3.0	13.4-13.5	36.9	45.8	2.5	3.1	0.4	0.5
7.3-7.4	92.2	116.8	15.3	19.0	2.5	3.1	13.5-13.6	31.5	39.6	2.1	2.7	0.3	0.4
7.4-7.5	98.6	123.3	16.0	19.8	2.5	3.1	13.6-13.7	27.0	33.3	1.8	2.2	0.3	0.4
7.5-7.6	103.6	130.4	16.4	20.3	2.6	3.3	13.7-13.8	22.6	27.9	1.5	1.9	0.3	0.3
7.6-7.7	108.6	138.2	16.9	20.9	2.7	3.3	13.8-13.9	18.7	23.3	1.2	1.5	0.2	0.2
7.7-7.8	115.1	145.0	17.1	21.6	2.7	3.4	13.9-14.0	15.2	19.1	1.0	1.2	0.2	0.2
7.8-7.9	120.5	152.6	17.8	21.7	2.8	3.4	14.0-14.1	12.2	15.2	0.8	1.0	0.1	0.2
7.9-8.0	126.3	159.7	17.8	22.0	2.9	3.5	14.1-14.2	9.5	12.0	0.6	0.8	0.1	0.1
8.0-8.1	131.9	166.7	18.2	22.5	2.9	3.6	14.2-14.3	7.4	9.2	0.5	0.6	0.1	0.1
8.1-8.2	137.7	172.1	18.4	22.8	3.0	3.6	14.3-14.4	5.7	7.0	0.3	0.4	0.1	0.1
8.2-8.3	143.2	179.2	18.9	23.2	3.0	3.7	14.4-14.5	4.4	5.2	0.3	0.3	0.0	0.1
8.3-8.4	148.8	186.0	19.0	23.5	3.0	3.7	14.5-14.6	3.2	4.0	0.2	0.2	0.0	0.0
8.4-8.5	153.7	193.3	19.3	23.9	3.1	3.8	14.6-14.7	2.4	3.1	0.2	0.2	0.0	0.0
8.5-8.6	159.0	199.2	19.6	24.0	3.1	3.9	14.7-14.8	1.8	2.1	0.1	0.1	0.0	0.0
8.6-8.7	164.0	205.5	19.6	24.3	3.1	3.9	14.8-14.9	1.3	1.5	0.1	0.1	0.0	0.0
8.7-8.8	168.2	211.5	19.6	24.6	3.1	3.9	14.9-15.0	0.9	1.1	0.1	0.1	0.0	0.0
8.8-8.9	172.6	216.6	20.0	24.8	3.2	3.9	15.0-15.1	0.7	0.8	0.0	0.1	0.0	0.0
8.9-9.0	177.2	222.1	20.0	24.7	3.2	4.0	15.1-15.2	0.4	0.6	0.0	0.0	0.0	0.0
9.0-9.1	181.6	226.8	20.1	25.1	3.2	3.9	15.2-15.3	0.2	0.3	0.0	0.0	0.0	0.0